ARTICLE

doi:10.1038/nature21373

Intragenic DNA methylation prevents spurious transcription initiation

Francesco Neri[1,2], Stefania Rapelli[3], Anna Krepelova[1,3], Danny Incarnato[1], Caterina Parlato[1], Giulia Basile[1], Mara Maldotti[1,3], Francesca Anselmi[1,3] & Salvatore Oliviero[1,3]

In mammals, DNA methylation occurs mainly at CpG dinucleotides. Methylation of the promoter suppresses gene expression, but the functional role of gene-body DNA methylation in highly expressed genes has yet to be clarified. Here we show that, in mouse embryonic stem cells, Dnmt3b-dependent intragenic DNA methylation protects the gene body from spurious RNA polymerase II entry and cryptic transcription initiation. Using different genome-wide approaches, we demonstrate that this Dnmt3b function is dependent on its enzymatic activity and recruitment to the gene body by H3K36me3. Furthermore, the spurious transcripts can either be degraded by the RNA exosome complex or capped, polyadenylated, and delivered to the ribosome to produce aberrant proteins. Elongating RNA polymerase II therefore triggers an epigenetic crosstalk mechanism that involves SetD2, H3K36me3, Dnmt3b and DNA methylation to ensure the fidelity of gene transcription initiation, with implications for intragenic hypomethylation in cancer.

DNA methylation of cytosine residues on CpGs is a heritable epigenetic modification crucial for mammalian development that involves the coordinated processes of DNA methylation, demethylation, and maintenance of the methylated cytosine[1–4]. *De novo* establishment of DNA methylation is regulated by the DNA methyltransferases Dnmt3a and Dnmt3b alone or in a complex with Dnmt3l, whereas DNA methylation maintenance is mediated by Dnmt1[5–9].

The methylation of gene promoters is associated with gene silencing, while the function of gene-body DNA methylation has not yet been clarified. Recent studies have reported that Dnmt3b binds preferentially to the gene bodies by interacting with the histone modification H3K36me3[10,11]. In this study, we took advantage of Dnmt3b specificity to target intragenic DNA methylation with the aim to clarify the function of DNA methylation within the gene body.

Dnmt3b loss reduces gene-body DNA methylation

To gain insight into the functional role of Dnmt3b-dependent intragenic DNA methylation, we generated two independent Dnmt3b knockout cell lines from mouse embryonic stem (ES) cell line E14 to exclude experimental artefacts due to different genetic backgrounds or prolonged cell culturing (Extended Data Fig. 1a–f). Next we investigated the distribution of endogenous Dnmt3b. ChIP-seq analysis revealed that endogenous intragenic Dnmt3b binding occurs preferentially on genes within the third and fourth quartiles of expression level and correlates with H3K36me3 histone modification (Fig. 1a–c and Extended Data Fig. 1g–q). Whole-genome bisulphite sequencing in wild-type or *Dnmt3b*$^{-/-}$ ES cells revealed a global reduction of genomic DNA methylation, with a significant decrease of the level of 5-methylcytosine (5mC) on exons and introns (Fig. 1d and Extended Data Fig. 1r). Genome splitting in deciles of H3K36me3 occupancy showed that both Dnmt3b binding and DNA methylation loss in *Dnmt3b*$^{-/-}$ cells strongly correlate with the abundance of H3K36me3 (Fig. 1e).

Analysis of intragenic spurious transcription

During transcriptional elongation, RNA polymerase II (Pol II) recruits the enzyme SetD2 to the transcribed region to carry out H3K36 trimethylation[12,13], which has been demonstrated to maintain a repressive chromatin environment to prevent spurious entry of Pol II[14]. In yeast, the repressive action of H3K36me3 is mediated by the recruitment of histone deacetylases (HDACs) that make the chromatin inaccessible[15]. Silencing of SetD2 in mammalian cells leads to cryptic transcription initiation of a large fraction of active genes. However, no change in histone acetylation levels occurs after SetD2 knockdown[12,14,16].

To investigate the functional role of the Dnmt3b-dependent DNA methylation on gene bodies, we performed a high-coverage total RNA-seq analysis in wild-type and *Dnmt3b*$^{-/-}$ ES cells (Extended Data Fig. 2a, b). The occurrence of cryptic intragenic transcription initiation was measured by the ratio between the RPKM (reads per kilobase per million mapped reads) of the intermediate exons and the RPKM of the first exon. *Dnmt3b*$^{-/-}$ cells displayed a significantly higher ratio from the second exon onwards (Fig. 2a). Of the total number of genes with an RPKM >1, 1,445 genes (18%) had a $\log_2$ ratio of intermediate exons versus first exon >1 (Fig. 2b). Analysis performed on technical and biological replicates, and validation by RT–qPCR (real-time quantitative polymerase chain reaction) on a subset of genes confirmed this result (Extended Data Fig. 2c–e). This indicates that in *Dnmt3b*$^{-/-}$ cells, a significant amount of RNAs are transcribed starting within the gene body.

Intragenic DNA methylation can regulate alternative promoters[17]. To test this hypothesis we investigated the promoter usage of genes that have two or more annotated alternative promoters. Even though the reactivation events of some alternative promoters were observed in *Dnmt3b*$^{-/-}$ cells, there was no evidence to suggest that Dnmt3b loss led to a general reactivation of these events at a genome-wide level (Extended Data Fig. 3).

Activation of cryptic intragenic transcription initiation events can be a consequence of spurious entry of Pol II into the gene body. To test this, we performed ChIP-seq analysis of Pol II and H3K36me3 in wild-type and *Dnmt3b*$^{-/-}$ cells. To distinguish between engaged and elongating Pol II, we treated the cells with 5,6-dichloro-1-β-D-ribofuranosylbenzimidazole (DRB), a chemical compound that inhibits transcription elongation[18,19]. We then performed ChIP-seq using two different antibodies recognizing either all Pol II or specifically

[1]Human Genetics Foundation (HuGeF), via Nizza 52, 10126 Torino, Italy. [2]Leibniz Institute on Aging – Fritz Lipmann Institute (FLI), Beutenbergstrasse 11, 07745 Jena, Germany. [3]Dipartimento di Scienze della Vita e Biologia dei Sistemi, Università di Torino, via Accademia Albertina 13, 10123 Torino, Italy.

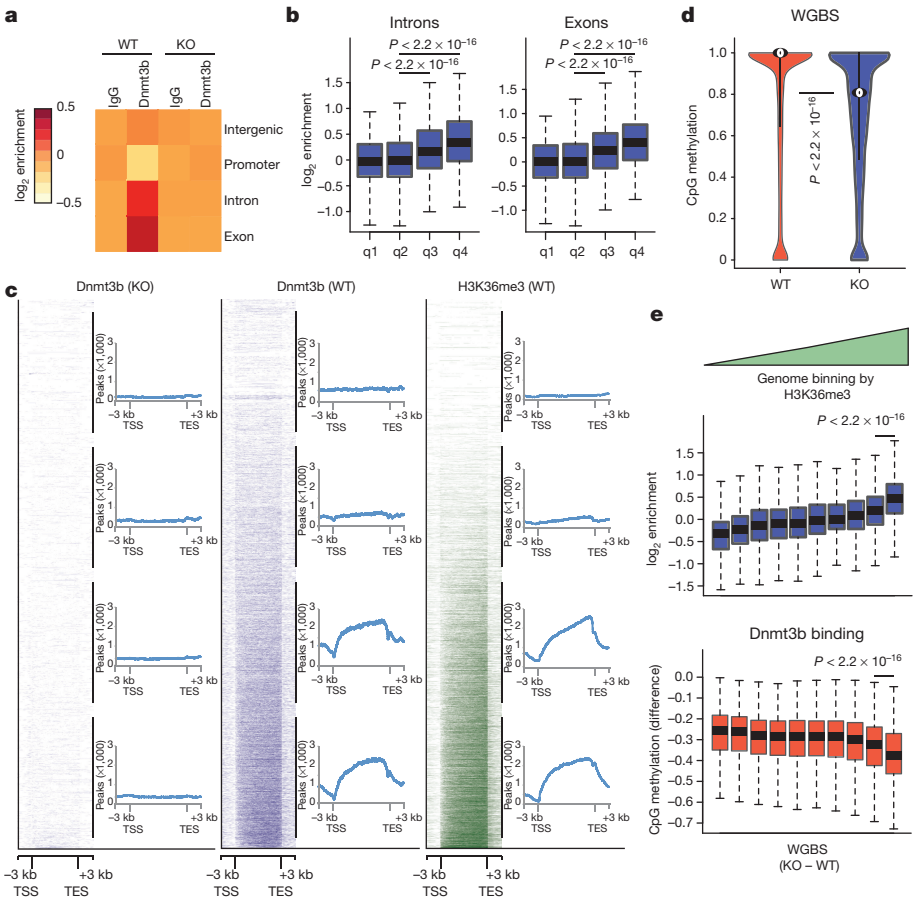

Figure 1 | Dnmt3b co-localizes with H3K36me3 on the gene body and its loss reduces gene-body DNA methylation. a, Binding enrichment of control IgG and endogenous Dnmt3b in wild-type (WT) and *Dnmt3b*$^{-/-}$ (KO) ES cells on the specified genomic features. **b**, Box plot of endogenous Dnmt3b binding on the introns and exons in ES cells partitioned in quartiles on the basis of the expression level (q4 = upper quartile, most expressed genes). Box indicates the interquartile range (IQR) and whiskers denote the 1.5 × IQR. **c**, Heat map of Dnmt3b and H3K36me3 distribution on genes (see Methods). TES, transcription end site. **d**, Violin plot of the methylation level of all CpGs by whole-genome bisulphite sequencing (WGBS). **e**, Genomic 500-bp bins divided in deciles depending on their H3K36me3 enrichment.

Pol II phosphorylated on serine 5 (Ser5); both antibodies are able to immunoprecipitate stalled Pol II (Extended Data Fig. 4a–c). We did not observe any significant changes in H3K36me3 and Pol II genomic profiles when comparing untreated wild-type to *Dnmt3b*$^{-/-}$ cells (Fig. 2c, d and Extended Data Fig. 4d–f). By contrast, we observed a significant increase of Pol II binding on intragenic regions when comparing *Dnmt3b*$^{-/-}$ to wild-type cells treated with DRB, using both antibodies. This was especially true of introns and exons of genes within the third and fourth quartiles of expression (Fig. 2c, d and Extended Data Fig. 4f) with a small but detectable increment of H3K4me3 and H3ac on genes belonging to the fourth quartile (the most highly expressed) (Extended Data Fig. 4g–j). These data strongly support the hypothesis that Dnmt3b is necessary to prevent spurious intragenic transcription initiation by repressing Pol II entry downstream of the canonical promoters.

To confirm the increase of intragenic transcription activation in *Dnmt3b*$^{-/-}$ cells, we performed RNA immunoprecipitation with a CAP-specific antibody[20] that was followed by high-throughput sequencing (CAPIP-seq) (Extended Data Fig. 5a–e). Application of this technique to total RNA showed a significant enrichment of the CAP signal in intermediate intronic and exonic regions of *Dnmt3b*$^{-/-}$ transcripts (Extended Data Fig. 5f-g).

Since Pol II ChIP-seq and CAPIP-seq are affinity-purification methods, which often display high background signal and are unable to map the transcription start sites (TSSs) at single-base resolution, we performed a high-throughput identification of the TSSs at single-base resolution in wild-type and *Dnmt3b*$^{-/-}$ cells. We used the RNA 5′ pyrophosphohydrolase (RppH) enzyme to decap eukaryotic mRNAs, leaving a 5′ monophosphate group[21] that was selectively used for adaptor ligation to map the CAP signals, transcriptome-wide (DECAP-seq) (Extended Data Fig. 6a–e). DECAP-seq analysis revealed a significant increase of TSSs on the gene bodies of genes within the third and fourth quartile of expression in *Dnmt3b*$^{-/-}$ cells compared to wild-type cells (Fig. 3a, b and Extended Data Fig. 6f, g). As the average RPM (reads per million mapped) value of each single-base TSS on annotated TSSs is around 6 (Extended Data Fig. 6h–j), we further analysed the single-base intragenic TSSs that had an RPM > 6. This analysis identified 2,627 highly expressed TSSs (RPM > 6) specific to *Dnmt3b*$^{-/-}$ cells, 780 TSSs common to both cell lines, and 936 specific to wild-type cells (Fig. 3c). The percentage of the total mapped reads specific to *Dnmt3b*$^{-/-}$ TSSs was 2.76%, while the percentage of common TSSs was 5.22%, suggesting that the latter represent canonical TSSs not present in the used gene annotation (Fig. 3d). The number of intragenic TSSs and the read distribution was similar in both DECAP-seq replicates, showing high overlap (Extended Data Fig. 6k–m), and were confirmed by significant enrichment of CAPIP-seq and Pol II ChIP-seq, as well as by an increased RNA-seq ratio between downstream and upstream exons in the knockout cells (Extended Data Fig. 6n–o).

The intragenic TSSs identified in *Dnmt3b*$^{-/-}$ cells were within genomic regions with significantly higher H3K36me3 and Dnmt3b binding, showed loss of methylation upon Dnmt3b depletion, and lower nucleosome occupancy with respect to randomly chosen intragenic regions (Fig. 3e). The final observation is in agreement with the recent finding of Dnmt3b enzymatic preference to the linker DNA[10,11].

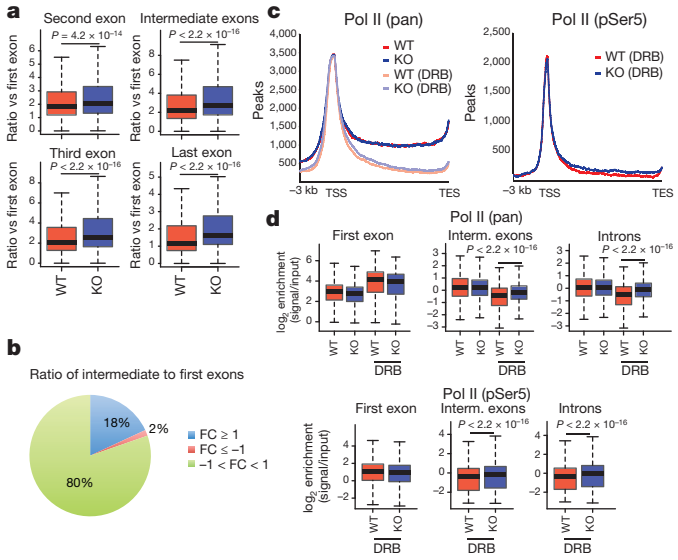

Figure 2 | Dnmt3b knockout increases intragenic RNA Pol II spurious entry and transcription initiation events on gene body. a, Box plot of the ratio between normalized RNA-seq read counts (RPKM) in wild-type and *Dnmt3b*$^{-/-}$ ES cells. *P* values calculated with Wilcoxon rank-sum test. **b**, Pie-chart showing the percentage of transcripts with fold change (FC) of ratio as indicated. $FC = \log_2\left[\frac{ratio_{KO}}{ratio_{WT}}\right]$ **c**, Plots of the pan (left panel) or phospho-Ser5 (right panel) RNA pol II distribution in wild-type and *Dnmt3b*$^{-/-}$ ES cells treated (or not, left panel) with DRB to inhibit Pol II elongation. **d**, Binding enrichment of pan (upper panel) or phospho-Ser5 (bottom panel) Pol II in wild-type and *Dnmt3b*$^{-/-}$ ES cells treated (or not, only pan Pol II) with DRB on the indicated genic features.

To get an insight into the mechanism that generates the cryptic intragenic transcripts, we next analysed the sequence context where the spurious intragenic TSSs are generated. It has been shown that mammalian transcription preferentially starts with a pyrimidine (C/T) at position −1 and with a purine (A/G) at position +1 (ref. 22). Our data confirm this observation on canonical TSSs, while on intragenic TSSs we observed the loss of the pyrimidine enrichment at position −1 and a reduced enrichment of the purine at position +1 (Fig. 3f). Notably, within a region of 50 base pairs centred at the Dnmt3b-dependent intragenic TSSs, we found a significant enrichment of the CpG dinucleotide and several transcription factor binding motifs containing CpG sequences, including motifs related to Sp1 and members of the Ets family (Fig. 3g, h and Extended data Fig. 7a). Since both Sp1 and Ets proteins can recruit the transcription machinery in TATA-less promoters, and their binding to the DNA is affected by CpG methylation[23–28], we verified the presence of their motifs on some example TSSs identified by the DECAP-seq analysis (Fig. 3i and Extended Data Fig. 7b).

First, we confirmed the presence of these cryptic TSSs with targeted CAP immunoprecipitation, Pol II ChIP and RT–qPCR by measuring the ratio between the downstream and upstream exon RNA of the intragenic TSSs and validated the differential methylation between wild-type and *Dnmt3b*$^{-/-}$ cells by using bisulphite Sanger sequencing (Extended Data Fig. 7c, d). We observed the enrichment of Tbp, TfIIb, Sp1, Elk1 and/or Elf1 by ChIP experiments on the cryptic TSSs, but not in the control region (Extended Data Fig. 7e).

Crosstalk between H3K36me3 and DNA methylation

To demonstrate the involvement of the H3K36me3 histone mark in this molecular event, we silenced SetD2 and measured the activation of cryptic TSSs in wild-type and *Dnmt3b*$^{-/-}$ cells. SetD2 knockdown resulted in a marked reduction of H3K36me3 both in wild-type and *Dnmt3b*$^{-/-}$ cells, and loss of Dnmt3b intragenic binding in wild-type cells (Fig. 4a–c and Extended Data Fig. 8a–f). The ratio of intermediate to first exons in SetD2-kncockout versus control cells showed an increase of spurious transcripts that was comparable to the increase measured in *Dnmt3b*$^{-/-}$ versus wild-type cells (Fig. 4d, e and Extended Data Fig. 8g, h). DECAP-seq revealed a significant increase of TSSs on the gene bodies of the transcripts of genes within the tope quartile of expression level in SetD2-silenced cells compared to control cells (Extended Data Fig. 8i–k). This analysis revealed 3,560 high confidence (RPM > 6) intragenic TSSs in SetD2-silenced cells, of which 2,759 were specific to SetD2 knockdown and more than 2,000 were in common with the TSSs identified in *Dnmt3b*$^{-/-}$ cells (Extended Data Figs 8l–o and 9a). Thus, Dnmt3b-mediated inhibition of spurious transcription initiation is dependent on the presence of H3K36me3.

Next we investigated whether this mechanism depends on the catalytic activity of Dnmt3b. Either the full-length wild-type Dnmt3b enzyme or the catalytically inactive mutant V725G (ref. 29) were expressed in *Dnmt3b*$^{-/-}$ cells (Fig. 4f). Both Dnmt3b proteins showed similar intragenic binding profiles (Fig. 4g, h and Extended Data Fig. 9b, c), although only the cells expressing the wild-type protein showed an increase in DNA methylation levels (Extended Data Fig. 9d, e). Total RNA-seq (Extended Data Fig. 9f, g) revealed a significant reduction in the ratio of intermediate to first exons in the cells expressing the wild-type Dnmt3b enzyme, but not in those expressing the Dnmt3b(V725G) mutant (Fig. 4i, j). To confirm the importance of the H3K36me3-mediated recruitment of the active Dnmt3b to the gene bodies further, we also used mutants (S277P and VW-RR) that are unable to bind H3K36me3 (Extended Data Fig. 9h)[10]. These Dnmt3b mutants showed lower intragenic binding with reduced DNA methylation activity (Extended Data Fig. 9i, j) and were unable to reduce the ratio of intermediate to first exons (Extended Data Fig. 10a–d). Thus, only the re-expression of the wild-type Dnmt3b was able to rescue the loss of spurious intragenic transcription initiation in *Dnmt3b*$^{-/-}$ cells, demonstrating that Dnmt3b-dependent DNA methylation is responsible for preventing the occurrence of cryptic intragenic transcription.

Analysis of spurious transcripts

Next, we analysed the fate of the cryptic RNAs generated by spurious intragenic initiation events. To this end we first analysed whether these RNAs are degraded. Silencing of the Dis3 and Rrp6 component of the RNA exosome complex did not result in changes to the total number of intragenic TSSs (Extended Data Fig. 10e–g), but did result in a significant increase in their expression level (Extended Data Fig. 10h–k), indicating that a fraction of the cryptic transcripts generated in *Dnmt3b*$^{-/-}$ cells are degraded by the RNA exosome complex. However, analysis of the poly(A)$^+$ transcripts by RNA-seq (Extended Data Fig. 10l, m) showed an increase in the ratio of intermediate to first exons in *Dnmt3b*$^{-/-}$ cells (Fig. 5a, b and Extended Data Fig. 10n, o), suggesting that the intragenic transcripts are, at least in part, polyadenylated.

To investigate the stability of these aberrant RNAs, and to follow their fate, we performed DECAP-seq upon poly(A)-enriched and cytoplasmic RNA. We found a significantly reduced number of intragenic TSSs in poly(A)$^+$ and cytosolic DECAP-seq with respect to DECAP-seq using total RNA (Extended Data Fig. 10p, q), confirming that a fraction of the spurious transcripts are actually degraded and indicating that not all cryptic transcripts undergo polyadenylation and nuclear export. Notably, almost all the highly expressed TSSs identified in *Dnmt3b*$^{-/-}$ cells can be found in the poly(A)$^+$ and cytosolic DECAP-seq fractions (Fig. 5c), albeit at a significantly lower level of expression with a consequent reduction in the percentage of the total mapped reads (Fig. 5d, e). The expression of highly expressed common TSSs does not globally change among the different cellular compartments (Extended Data Fig. 10r, s).

To measure the stability of the poly(A)$^+$ cryptic RNAs further, we estimated the mRNA half-life in wild-type and *Dnmt3b*$^{-/-}$ cells by performing poly(A)$^+$ RNA-seq analyses in DRB-treated cells at different time points[30] (Extended Data Fig. 11a, b). The intronic RNA inclusion in *Dnmt3b*$^{-/-}$ cells remained consistently higher than in wild-type cells at all time points (Fig. 5f) and the intronic RNA half-life slightly increased

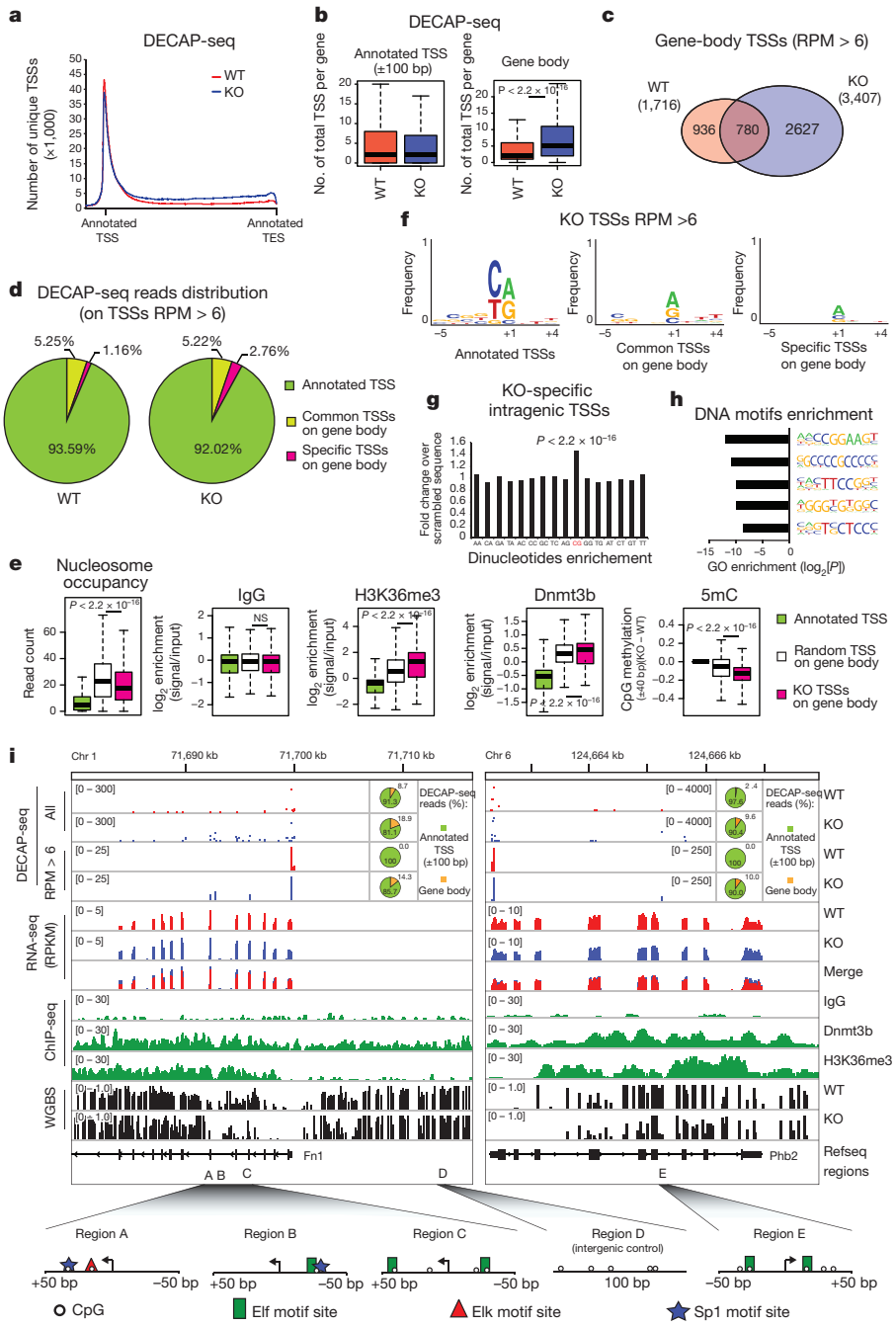

Figure 3 | Dnmt3b is required to maintain transcription initiation fidelity. a, **b**, Total TSS distribution along genes in *Dnmt3b*$^{-/-}$ compared with wild-type ES cells. **c**, Venn diagram of intragenic TSSs with a DECAP-seq signal (RPM) > 6. Overlap is calculated at single-base resolution. **d**, Pie-charts of the DECAP-seq reads distribution on TSSs with RPM > 6 in wild-type and *Dnmt3b*$^{-/-}$ cells. **e**, Box plot distribution of the IgG, Dnmt3b, and H3K36me3 ChIP-seq signal enrichment as well as of the DNA methylation ratio between *Dnmt3b*$^{-/-}$ and wild-type ES cells (from whole-genome bisulphite sequencing) and nucleosome occupancy of the novel identified TSSs. NS, not significant. **f**, Sequence logo for genomic region sequences of the TSSs identified by DECAP-seq experiments in *Dnmt3b*$^{-/-}$ and wild-type ES cells. **g**, **h**, Histogram plot of observed over expected ratio showing a specific enrichment of CpG dinucleotides in a region around 25 nucleotides of TSSs specific to *Dnmt3b*$^{-/-}$ cells and a significant enrichment of CpG-containing motifs in intragenic TSSs specific to *Dnmt3b*$^{-/-}$ ES cells. **i**, Top, genomic view of the *Fn1* and *Phb2* genes showing intragenic transcription initiation events. Pie charts indicate the DECAP-seq read distribution in *Dnmt3b*$^{-/-}$ and wild-type ES cells. WGBS, whole-genome bisulphite sequencing. Bottom, schematic representation of CpG localization and putative transcription factor binding elements. *P* values calculated with Wilcoxon rank-sum test (**b**, **e**) and by χ^2 test (**g**).

in *Dnmt3b*$^{-/-}$ cells (Extended Data Fig. 11d, f), whereas the whole-transcriptome half-life did not show any significant difference between wild-type and *Dnmt3b*$^{-/-}$ cells (Extended Data Fig. 11c, e, g). Moreover, the ratio of intermediate to first exons was higher in *Dnmt3b*$^{-/-}$ cells than in wild-type cells at all time points of DRB treatment (Fig. 5g, h), revealing that the spurious RNAs, once polyadenylated, are as stable as the full-length RNAs transcribed from canonical TSSs.

To characterize the biological impact of the cryptic transcripts we investigated their post-transcriptional processing by performing mRNA ribosome profiling[31] (Extended Data Fig. 11h, i). Active mRNA translation sequencing (ART-seq) revealed that *Dnmt3b*$^{-/-}$ cells displayed a significant reduction in ribosome occupancy at the 5′ untranslated region, together with a marked increase in the occupancy of RNA intronic regions, especially on genes within the top

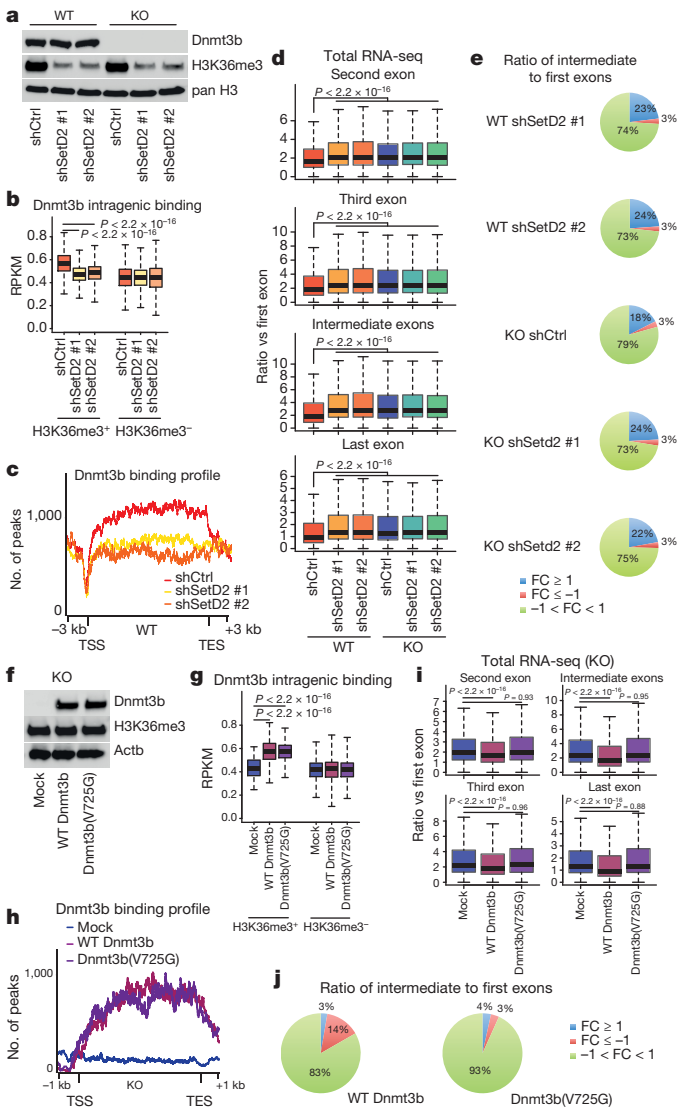

Figure 4 | H3K36me3-dependent maintenance of transcription initiation fidelity is mediated by Dnmt3b through its DNA methylation activity. a, Western blotting analysis of control (shCtrl) or SetD2 (shSetD2 #1/2) knockdowns in wild-type and *Dnmt3b*$^{-/-}$ ES cells. sh, short hairpin. **b**, Box plot of normalized Dnmt3b ChIP-seq read counts (RPKM) in control or shSetD2 wild-type cells on H3K36me3-negative and H3K36me3-positive genes. **c**, Dnmt3b distribution on genes in control or shSetD2 cells. **d**, Box plot of the ratio between normalized RNA-seq RPKM in wild-type and *Dnmt3b*$^{-/-}$ control or shSetD2 ES cells. **e**, Pie charts showing the percentage of transcripts with the indicated fold change (FC), where $\mathrm{FC} = \log_2\left[\frac{\mathrm{ratio}_1}{\mathrm{ratio}_{\mathrm{WTshCtrl}}}\right]$. Ratio_1 is the ratio of the condition stated in the panel. **f**, Western blot of *Dnmt3b*$^{-/-}$ ES cells transfected with mock, wild-type Dnmt3b or inactive Dnmt3b(V725G). **g**, Box plot of normalized Dnmt3b ChIP-seq RPKM in *Dnmt3b*$^{-/-}$ ES cells transfected as indicated. **h**, Dnmt3b distribution on genes in *Dnmt3b*$^{-/-}$ ES cells transfected as indicated. **i**, Box plot of the ratio between normalized RNA-seq RPKM in *Dnmt3b*$^{-/-}$ ES cells transfected as indicated. **j**, Pie charts showing the percentage of transcripts with the indicated fold change. $\mathrm{FC} = \log_2\left[\frac{\mathrm{ratio}_1}{\mathrm{ratio}_{\mathrm{KO\,mock}}}\right]$, where ratio_1 is the ratio of intermediate to first exons in *Dnmt3b*$^{-/-}$ ES cells treated with either wild-type Dnmt3b or inactive Dnmt3b(V725G), as indicated. *P* values calculated with Wilcoxon rank-sum test (**b**, **d**, **g**, **e**).

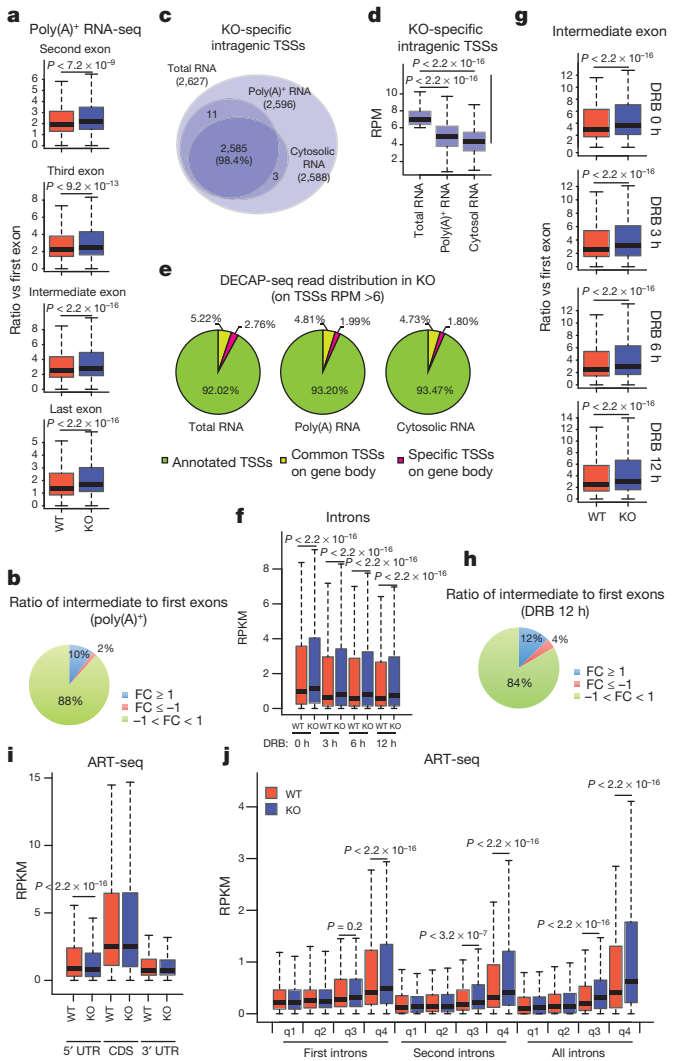

Figure 5 | Transcripts produced from intragenic cryptic starting sites are polyadenylated, stable and ribosome-associated RNAs. a, Box plot of the ratio between normalized poly(A) RNA-seq RPKM in wild-type and *Dnmt3b*$^{-/-}$ ES cells. **b**, Pie chart showing the percentage of transcripts with the indicated fold change. Fold change is defined as in Fig. 2b. **c**, Venn diagram of the intragenic TSSs specific to *Dnmt3b*$^{-/-}$ cells(RPM > 6) in the indicated RNA compartments. **d**, Box plot of normalized DECAP-seq RPM on intragenic TSSs specific to *Dnmt3b*$^{-/-}$ ES cells in the indicated RNA compartments. **e**, Pie chart of the DECAP-seq read distribution. **f**, Box plot of the RPKM counts on introns in cells (wild-type and *Dnmt3b*$^{-/-}$) treated with DRB. **g**, Box plot of the ratio between normalized poly(A)$^+$ RNA-seq RPKM in wild-type and *Dnmt3b*$^{-/-}$ ES cells treated with DRB for 12 h. **h**, Pie chart showing the percentage of transcripts in cells treated with DRB for 12 h with the indicated fold change. Fold change is defined as in Fig. 2b. **i**, Box plot of the normalized ART-seq RPKM on the indicated RNA regions. UTR, untranslated region. CDS, coding DNA sequence. **j**, Box plot of the normalized ART-seq RPKM on the indicated classes of introns divided into quartiles (q1–q4) according to the level of gene expression. *P* values calculated with Wilcoxon rank-sum test (**a**, **d**, **g**, **f**, **i**, **j**).

quartile of expression level (Fig. 5i, j and Extended Data Fig. 11j, k). We did not observe significant changes in ribosome enrichment of the coding region of the transcripts between wild-type and *Dnmt3b*$^{-/-}$ cells (Fig. 5i and Extended Data Fig. 11j). Together, these results suggest that increasing Pol II spurious entry and consequent transcription of cryptic RNAs might generate aberrant proteins.

Discussion

DNA methylation takes place both at the promoters and within the gene body. While it is well-documented that DNA methylation at the promoters is associated with gene silencing, the function of gene-body DNA methylation remains elusive. Here we demonstrate that Dnmt3b-dependent DNA methylation on the gene body is responsible for the

prevention of aberrant transcription initiation events necessary to guarantee the fidelity of mRNA transcription initiation (Extended Data Fig. 12a). Previous studies reported examples of alternative splicing or activation of retroviruses due to intragenic DNA methylation[32–34]. We tested these hypotheses and, in agreement with the literature, we found few events of alternative splicing or activation of repetitive elements occurring in *Dnmt3b*$^{-/-}$ cells (data not shown). However, these regulations were sporadic in our model.

Our work, unveiling the functional role of the epigenetic crosstalk between Pol II, H3K36me3, and DNA methylation (Extended Data Fig. 12b), can explain physiological gene regulation as well as the occurrence of abnormal transcripts in cancer. Indeed, global DNA hypomethylation, especially on intragenic regions, is a general feature of most tumours[35–37]. Moreover, several recent studies reported the loss or mutation of SETD2 and the consequent loss of H3K36me3 histone marks as a key event in promoting cancer growth and malignancy[38–40]. This work reveals a novel function of intragenic DNA methylation and provides new aspects that have to be considered when evaluating the roles of SETD2 and DNMT3B in cancer establishment and progression. Partial internal RNAs generated by the loss of transcription initiation fidelity could affect multiple biological processes, impairing molecular mechanisms such as regulation of gene expression, miRNA targeting, truncated protein generation and others, thus favouring (stochastic) tumour cell heterogeneity and neoplastic predisposition.

Online Content Methods, along with any additional Extended Data display items and Source Data, are available in the online version of the paper; references unique to these sections appear only in the online paper.

Received 10 September 2015; accepted 5 January 2017.
Published online 22 February 2017.

1. Robertson, K. D. DNA methylation, methyltransferases, and cancer. *Oncogene* **20,** 3139–3155 (2001).
2. Chen, Z. X. & Riggs, A. D. DNA methylation and demethylation in mammals. *J. Biol. Chem.* **286,** 18347–18353 (2011).
3. Neri, F. *et al.* Single-base resolution analysis of 5-formyl and 5-carboxyl cytosine reveals promoter DNA methylation dynamics. *Cell Reports* **10,** 674–683 (2015).
4. Neri, F. *et al.* TET1 is a tumour suppressor that inhibits colon cancer growth by derepressing inhibitors of the WNT pathway. *Oncogene* **34,** 4168–4176 (2015).
5. Okano, M., Bell, D. W., Haber, D. A. & Li, E. DNA methyltransferases Dnmt3a and Dnmt3b are essential for *de novo* methylation and mammalian development. *Cell* **99,** 247–257 (1999).
6. Bestor, T. H. The DNA methyltransferases of mammals. *Hum. Mol. Genet.* **9,** 2395–2402 (2000).
7. Schübeler, D. Function and information content of DNA methylation. *Nature* **517,** 321–326 (2015).
8. Jeltsch, A. & Jurkowska, R. Z. New concepts in DNA methylation. *Trends Biochem. Sci.* **39,** 310–318 (2014).
9. Neri, F. *et al.* Dnmt3L antagonizes DNA methylation at bivalent promoters and favors DNA methylation at gene bodies in ESCs. *Cell* **155,** 121–134 (2013).
10. Baubec, T. *et al.* Genomic profiling of DNA methyltransferases reveals a role for DNMT3B in genic methylation. *Nature* **520,** 243–247 (2015).
11. Morselli, M. *et al. In vivo* targeting of *de novo* DNA methylation by histone modifications in yeast and mouse. *eLife* **4,** e06205 (2015).
12. Edmunds, J. W., Mahadevan, L. C. & Clayton, A. L. Dynamic histone H3 methylation during gene induction: HYPB/Setd2 mediates all H3K36 trimethylation. *EMBO J.* **27,** 406–420 (2008).
13. Yoh, S. M., Lucas, J. S. & Jones, K. A. The Iws1:Spt6:CTD complex controls cotranscriptional mRNA biosynthesis and HYPB/Setd2-mediated histone H3K36 methylation. *Genes Dev.* **22,** 3422–3434 (2008).
14. Wagner, E. J. & Carpenter, P. B. Understanding the language of Lys36 methylation at histone H3. *Nat. Rev. Mol. Cell Biol.* **13,** 115–126 (2012).
15. Carrozza, M. J. *et al.* Histone H3 methylation by Set2 directs deacetylation of coding regions by Rpd3S to suppress spurious intragenic transcription. *Cell* **123,** 581–592 (2005).
16. Carvalho, S. *et al.* Histone methyltransferase SETD2 coordinates FACT recruitment with nucleosome dynamics during transcription. *Nucleic Acids Res.* **41,** 2881–2893 (2013).
17. Maunakea, A. K. *et al.* Conserved role of intragenic DNA methylation in regulating alternative promoters. *Nature* **466,** 253–257 (2010).
18. Maderious, A. & Chen-Kiang, S. Pausing and premature termination of human RNA polymerase II during transcription of adenovirus *in vivo* and *in vitro*. *Proc. Natl Acad. Sci. USA* **81,** 5931–5935 (1984).
19. Yankulov, K., Yamashita, K., Roy, R., Egly, J. M. & Bentley, D. L. The transcriptional elongation inhibitor 5,6-dichloro-1-β-D-ribofuranosylbenzimidazole inhibits transcription factor IIH-associated protein kinase. *J. Biol. Chem.* **270,** 23922–23925 (1995).
20. Bochnig, P., Reuter, R., Bringmann, P. & Lührmann, R. A monoclonal antibody against 2,2,7-trimethylguanosine that reacts with intact, class U, small nuclear ribonucleoproteins as well as with 7-methylguanosine-capped RNAs. *Eur. J. Biochem.* **168,** 461–467 (1987).
21. Deana, A., Celesnik, H. & Belasco, J. G. The bacterial enzyme RppH triggers messenger RNA degradation by 5′ pyrophosphate removal. *Nature* **451,** 355–358 (2008).
22. Carninci, P. *et al.* Genome-wide analysis of mammalian promoter architecture and evolution. *Nat. Genet.* **38,** 626–635 (2006).
23. Butler, J. E. F. & Kadonaga, J. T. The RNA polymerase II core promoter: a key component in the regulation of gene expression. *Genes Dev.* **16,** 2583–2592 (2002).
24. Clark, S. J., Harrison, J. & Molloy, P. L. Sp1 binding is inhibited by ^{m}Cp^{m}CpG methylation. *Gene* **195,** 67–71 (1997).
25. Douet, V., Heller, M. B. & Le Saux, O. DNA methylation and Sp1 binding determine the tissue-specific transcriptional activity of the mouse Abcc6 promoter. *Biochem. Biophys. Res. Commun.* **354,** 66–71 (2007).
26. Hogart, A. *et al.* Genome-wide DNA methylation profiles in hematopoietic stem and progenitor cells reveal overrepresentation of ETS transcription factor binding sites. *Genome Res.* **22,** 1407–1418 (2012).
27. Uchiumi, F., Miyazaki, S. & Tanuma, S. The possible functions of duplicated ets (GGAA) motifs located near transcription start sites of various human genes. *Cell. Mol. Life Sci.* **68,** 2039–2051 (2011).
28. Yu, M. *et al.* GA-binding protein-dependent transcription initiator elements. Effect of helical spacing between polyomavirus enhancer a factor 3(PEA3)/Ets-binding sites on initiator activity. *J. Biol. Chem.* **272,** 29060–29067 (1997).
29. Gowher, H. & Jeltsch, A. Molecular enzymology of the catalytic domains of the Dnmt3a and Dnmt3b DNA methyltransferases. *J. Biol. Chem.* **277,** 20409–20414 (2002).
30. Tani, H. & Akimitsu, N. Genome-wide technology for determining RNA stability in mammalian cells: historical perspective and recent advantages based on modified nucleotide labeling. *RNA Biol.* **9,** 1233–1238 (2012).
31. Ingolia, N. T., Lareau, L. F. & Weissman, J. S. Ribosome profiling of mouse embryonic stem cells reveals the complexity and dynamics of mammalian proteomes. *Cell* **147,** 789–802 (2011).
32. Maunakea, A. K., Chepelev, I., Cui, K. & Zhao, K. Intragenic DNA methylation modulates alternative splicing by recruiting MeCP2 to promote exon recognition. *Cell Res.* **23,** 1256–1269 (2013).
33. Yearim, A. *et al.* HP1 is involved in regulating the global impact of DNA methylation on alternative splicing. *Cell Reports* **10,** 1122–1134 (2015).
34. Jones, P. A. Functions of DNA methylation: islands, start sites, gene bodies and beyond. *Nat. Rev. Genet.* **13,** 484–492 (2012).
35. Jones, P. A. & Baylin, S. B. The fundamental role of epigenetic events in cancer. *Nat. Rev. Genet.* **3,** 415–428 (2002).
36. Gaudet, F. *et al.* Induction of tumors in mice by genomic hypomethylation. *Science* **300,** 489–492 (2003).
37. Feinberg, A. P. & Vogelstein, B. Hypomethylation distinguishes genes of some human cancers from their normal counterparts. *Nature* **301,** 89–92 (1983).
38. Kanu, N. *et al.* SETD2 loss-of-function promotes renal cancer branched evolution through replication stress and impaired DNA repair. *Oncogene* **34,** 5699–5708 (2015).
39. Fontebasso, A. M. *et al.* Mutations in *SETD2* and genes affecting histone H3K36 methylation target hemispheric high-grade gliomas. *Acta Neuropathol.* **125,** 659–669 (2013).
40. Duns, G. *et al.* Histone methyltransferase gene *SETD2* is a novel tumor suppressor gene in clear cell renal cell carcinoma. *Cancer Res.* **70,** 4287–4291 (2010).

Supplementary Information is available in the online version of the paper.

Acknowledgements We thank T. Baubec and D. Schübeler for providing the Dnmt3b construct. We thank S. Yamanaka for anti-Dnmt3l antibody. We thank E. Guccione, R. Calogero and T. Bates for helpful suggestions and critical reading of the manuscript. This work was supported by the Associazione Italiana Ricerca sul Cancro (AIRC) IG 2014 Id15217.

Author Contributions F.N. and S.O. conceived the study; S.R. and A.K. performed genome-wide experiments, cloning and cell treatments; F.N. and D.I. performed genome-wide experiments and data analysis; M.M. performed cloning and cell treatments; C.P. and G.B. performed RNA-seq; F.A. performed CAPIP-seq experiments; F.N. and S.O. wrote the paper with input from all authors.

Author Information Reprints and permissions information is available at www.nature.com/reprints. The authors declare no competing financial interests. Readers are welcome to comment on the online version of the paper. Correspondence and requests for materials should be addressed to S.O. (salvatore.oliviero@unito.it) and F.N. (francesco.neri@leibniz-fli.de).

Reviewer Information *Nature* thanks P. Carninci and the other anonymous reviewer(s) for their contribution to the peer review of this work.

METHODS

No statistical methods were used to predetermine sample size. The experiments were not randomized and the investigators were not blinded to allocation during experiments and outcome assessment.

Cell culture. E14 mouse ES cells were cultured in high-glucose DMEM (Invitrogen) supplemented with 15% FBS (Millipore), 0.1 mM non-essential amino acids (Invitrogen), 1 mM sodium pyruvate (Invitrogen), 0.1 mM 2-mercaptoethanol, 1500 U ml^{-1} LIF (Millipore), 25 U ml^{-1} penicillin, and 25 μg ml^{-1} streptomycin. The cells were mycoplasma free.

Generation of *Dnmt3b*$^{-/-}$ ES cells was performed using TALEN technology. Cells were transfected with the two TALEN constructs targeting exon 17 of murine *Dnmt3b* (corresponding to the start of the catalytic domain) and after 16 h were seeded as a single cell. After ten days, clones were screened by western blot analysis. Positive clones were analysed by genomic sequencing.

For half-life measurements and Pol II elongation inhibition, wild-type and *Dnmt3b*$^{-/-}$ ES cells were treated with DRB at the concentration of 75 μM for the indicated times.

Protein extraction and western blotting. For total cell extracts, cells were resuspended in F-buffer (10 mM Tris-HCl pH 7.0, 50 mM NaCl, 30 mM Na-pyrophosphate, 50 mM NaF, 1% Triton X-100, anti-proteases) and sonicated for three pulses. Extracts were quantified using BCA assay (Pierce) and were run on SDS-polyacrylamide gels at different percentages, transferred to nitrocellulose membranes and incubated with specific primary antibodies overnight.

Nuclear protein extractions were performed as described in ref. 41. In brief, cells were harvested in PBS 1× and resuspended in isotonic buffer (20 mM HEPES pH 7.5, 100 mM NaCl, 250 mM sucrose, 5 mM $MgCl_2$, 5 μM $ZnCl_2$). Successively, cells were resuspended in isotonic buffer supplemented with 1% NP-40 to isolate nuclei. The isolated nuclei were resuspended in digestion buffer (50 mM Tris-HCl pH 8.0, 100 mM NaCl, 250 mM sucrose, 0.5 mM $MgCl_2$, 5 mM $CaCl_2$, 5 μM $ZnCl_2$) and treated with Micrococcal Nuclease (NEB) at 30 °C for 10 min.

Immunoprecipitation. Nuclear proteins from about 1×10^7 cells were incubated with 3 μg of specific antibody overnight at 4 °C. Immunocomplexes were incubated with protein-G-conjugated magnetic beads (DYNAL, Invitrogen) for 2 h at 4 °C. Samples were washed four times with digestion buffer supplemented with 0.1% NP-40 at RT. Proteins were eluted by incubating with 0.4 M NaCl TE buffer for 30 min and were analysed by western blotting.

DNA construct and shRNA. Custom shRNAs against SetD2, Dis3 and Rrp6 were constructed using the TRC hairpin design tool (http://www.broadinstitute.org/rnai/public/seq/search), and designed to target the 3′ UTR. shRNAs with more than 14 consecutive matches to non-target transcripts were avoided. Hairpins were cloned into pLKO.1 vector (Addgene: 10878) and each construct was verified by sequencing. Dnmt3b construct was obtained by PCR amplification and cloned into pEF6/V5-His vector (Invitrogen). The Dnmt3b mutant constructs (V725G, S277P and VW-RR) were generated by introducing a site-specific mutation in the DNA sequence corresponding to Val725 to mutate it into a glycine, or Ser277 to mutate it into a proline, or Val236Trp237 to mutate it to Arg–Arg, using QuickChange XL Site-Directed Mutagenesis Kit (Agilent Technologies).

Transfections. Transfections of mouse ES cells were performed using Lipofectamine 2000 Transfection Reagent in according to manufacturer's protocol using equal amounts of each plasmid in multiple transfections. For SetD2 knockdown, cells were transfected with 5 μg of the specific shRNA construct, and maintained in medium with puromycin selection (1 μg ml^{-1}) for 48 h.

Chromatin immunoprecipitation assay. To investigate the distribution of the endogenous Dnmt3b we tested different antibodies and found one that was able to immunoprecipitate the endogenous Dnmt3b cross-linked to chromatin, which showed no background signal in *Dnmt3b*$^{-/-}$ (Extended Data Fig. 1g–i). The ChIP-seq data were validated by ChIP–qPCR, using several biological replicates, on target genomic regions and by crosslinked co-immunoprecipitation experiments between Dnmt3b and H3K36me3 in wild-type or *Dnmt3b*$^{-/-}$ ES cells (Extended Data Fig. 1o, p). For Dnmt3b ChIP-seq, approximately 2×10^7 cells were cross-linked by addition of formaldehyde to 1% for 10 min at RT, quenched with 0.125 M glycine for 5 min at RT, and then washed twice with cold PBS. The cells were resuspended in lysis buffer 1 (50 mM HEPES-KOH pH 7.5, 140 mM NaCl, 1 mM EDTA, 10% glycerol, 0.5% NP-40, 0.25% Triton X-100 and protease inhibitor) to disrupt the cell membrane and in lysis buffer 2 (10 mM Tris-HCl pH 8.0, 200 mM NaCl, 1 mM EDTA, 0.5 mM EGTA and protease inhibitor) to isolate nuclei. The isolated nuclei were then resuspended in SDS ChIP Buffer (20 mM Tris-HCl pH 8.0, 10 mM EDTA, 1% SDS and protease inhibitors). Extracts were sonicated using the BioruptorH Twin (Diagenode) for two runs of ten cycles (30 s on, 30 s off) at high-power setting. Cell lysate was centrifuged at 12,000*g* for 10 min at 4 °C. The supernatant was diluted with ChIP dilution buffer (20 mM Tris-HCl pH 8.0, 150 mM NaCl, 2 mM EDTA, 1% Triton) before the immunoprecipitation step. Magnetic beads (Dynabeads rat anti-mouse IgM for anti-Pol II-phospho-S5, Dynabeads Protein G for all the other ChIPs, Life Technologies) were saturated with PBS/1% BSA and the samples were incubated with 2 μg of antibody overnight at 4 °C on a rotator. Next day samples were incubated with saturated beads for two hours at 4 °C on a rotator. Successively immunoprecipitated complexes were washed five times with RIPA buffer (50 mM HEPES-KOH pH 7.6, 500 mM LiCl, 1 mM EDTA, 1% NP-40, 0.7% Na-Deoxycholate) at 4 °C for 5 min each on a rotator. For other ChIP-seq, ChIP-seq was performed as described previously[42]. Elution buffer was added and incubated at 65 °C for 15 min. The de-crosslinking was performed at 65 °C overnight. De-crosslinked DNA was purified using QiaQuick PCR Purification Kit (Quiagen) according to the manufacture's instruction.

MeDIP was performed using MeDIP kit (Active Motif), according to the manufacturer's protocol.

DNA was analysed by quantitative real-time PCR by using SYBR GreenER kit (Invitrogen). All experiment values were normalized to input. The data shown represent triplicate real-time quantitative PCR measurements of the immunoprecipitated DNA. The data are expressed as a percentage of the DNA inputs. Error bars represent standard deviation determined from triplicate experiments. Oligonucleotide sequences are reported in Supplementary Table 1.

DNA extraction and dot-blot analysis. Genomic DNA was extracted from cells using DNeasy Blood and Tissue kit (Qiagen). For dot-blot analysis, extracted genomic DNA was sonicated using the BioruptorH Twin (Diagenode) for two runs of ten cycles (30 s on, 30 s off) at high-power setting, in order to obtain 300-bp fragments, denatured with 0.4 M NaOH and incubated for 10 min at 95 °C before being spotted onto HybondTM-N+ (GE Healthcare). Membranes were saturated with 5% milk and incubated with the specific antibodies overnight.

ChIP-seq library preparation. Approximately 10 ng of purified ChIP DNA were end-repaired, dA-tailed, and adaptor-ligated using the NEBNext ChIP-seq Library Prep Master Mix Set (NEB), following the manufacturer's instructions.

Whole genome bisulphite-seq library preparation. For whole-genome bisulphite-seq library preparation, 2.5 μg of ES cells genomic DNA, were spiked-in with 1 ng of *Escherichia coli* genomic DNA, and sheared using a Bioruptor Twin sonicator (Diagenode) for three runs of ten cycles (30 s on, 30 s off) at high-power setting. Fragmented/digested DNA was then end-repaired, dA-tailed, and ligated to methylated adapters, using the Illumina TruSeq DNA Sample Prep Kit, following manufacturer instructions. DNA was loaded on EGel Size select 2% agarose pre-cast gel (Invitrogen), and a fraction corresponding to fragments ranging from 180 bp to 350 bp was recovered. Purified DNA was then subjected to bisulphite conversion using the EpiTect Bisulphite Kit (Qiagen). Bisulphite-converted DNA was finally enriched by 15 cycles of PCR using Pfu Turbo Cx HotStart Taq (Agilent).

RNA extraction and RT–PCR analysis. Total RNA was extracted as previously described[43] using TRIzol reagent (Invitrogen). Real-time PCR was performed using the SuperScript III Platinum One-Step Quantitative RT–PCR System (Invitrogen) following the manufacturer's instructions.

RNA-seq library preparation. Ribo-RNA-seq library preparation was performed as described previously[44]. In brief, 2.5 μg of total RNA were depleted of ribosomal RNA using the RiboMinus Eukaryote System v2 kit (Invitrogen), following manufacturer instructions. Ribo-RNA was resuspended in 17 μl of EFP buffer (Illumina), heated to 94 °C for 8 min, and used as input for first strand synthesis, using the TruSeq RNA Sample Prep kit, following manufacturer instructions. Poly(A) RNA-seq library was performed by using the TruSeq RNA Sample Prep kit, following the manufacturer's instructions.

CAPIP-seq immunoprecipitation and library preparation. For immunoprecipitation of mRNA for CAP-Seq experiments, 30 μg of total RNA were fragmented by alkaline hydrolysis in ~200-nt fragments and incubated with 5 μg of mouse anti-CAP antibody (anti-m3G-cap, m7g-cap, Clone H20, Millipore MABE419) (or IgG) overnight at 4 °C in 0.5 ml of IP buffer (10 mM Tris-HCl pH 7.5; 150 mM NaCl; 0.1% Triton X-100) supplemented with 50 U ml^{-1} RNaseOUT (Invitrogen), 50 U ml^{-1} SuperaseIN (Invitrogen), and 50 U ml^{-1} RNase Inhibitor (Ambion). 25 μl of Dynabeads Protein G (Invitrogen) were saturated overnight at 4 °C in IP buffer supplemented with 150 μg of Sonicated Salmon Sperm DNA (Qiagen). Following incubation, beads were washed two times in IP buffer and incubated with the preformed RNA-antibody complexes at 4 °C. After 3 h, beads were washed four times with IP buffer. Specific elution of recovered fragments were obtained by incubation of beads with 100 μl elution buffer (5 mM Tris pH 7.5; 1 mM EDTA; 0.05% SDS; 0.3 mg ml^{-1} Proteinase K) for 1.5 h at 50 °C. Fragments were then purified by addition of 1 ml of TRIzol reagent (Invitrogen), and subjected to random-primed reverse transcription using the SuperScript III Reverse Trancriptase (Invitrogen) at 50 °C for 1 h. Resulting cDNAs were then used as input for the TruSeq RNA Sample Prep kit (Illumina), starting from the 'second strand synthesis' step, to produce the sequencing library, following the manufacturer's instruction.

DECAP-seq library preparation. To map the transcriptional start sites at single-base resolution we used an enzymatic-based approach by the use of the RNA 5′ pyrophosphohydrolase (RppH) enzyme to decap eukaryotic mRNAs[21]. We validated the specificity of this technique in a pilot experiment by comparing RppH-treated RNA versus untreated or T4 polynucleotide kinase (PNK)-treated RNA (Extended Data Fig. 6a–e).

When required the total RNA was depleted from small nuclear RNAs (snRNAs) by using the following protocol. 5 μg of total RNA was resuspended in snRNA-depletion buffer (20 mM HEPES pH 7.5, 80 mM KCl, 1 mM DTT), 1 μl RNase inhibitor (Ambion), 2 μM oligo mix (designed against snRNAs sequences, primers sequences in Supplementary Table 1) in a final volume of 50 μl, heated to 70 °C for 5 min and immediately put on ice. After that it was added 25 μl snRNA-depletion buffer 2 × (40 mM HEPES pH 7.5, 160 mM KCl, 10 mM $MgCl_2$, 2 mM DTT), supplemented with 1 μl RNase inhibitor (Ambion) and 1 μl of RNAse H (NEB) to a final volume of 100 μl. Incubated for 30 min at 37 °C. snRNA-depleted RNA were purified by RNA Clean and Concentration kit (Zymo Research) and DNaseI digestion was performed following the manufacturer's instructions. snRNA-depleted RNAs were further depleted from ribosomal RNA by using the RiboMinus Eukaryote System v2 kit (Invitrogen).

The RNA obtained from previous depletions (or poly(A)$^+$ RNA enriched using NEBNext Poly(A) mRNA Magnetic Isolation Module kit (NEB), following the manufacturer's instructions) was chemically fragmented by using first strand buffer of the SuperScript II Reverse Transcriptase (Invitrogen). The fragmented RNA was dephosphorylated of natural 5′ and fragmentation-derived 3′ phosphate by using Antarctic Phosphatase (AP, NEB). Dephosphorylated RNA was then treated with RNA 5′ pyrophosphohydrolase (RppH, NEB) in 1 × Thermopol buffer (NEB) (for decapping and pyrophosphate removal from the 5′ end of RNA to leave a 5′ monophosphate RNA). For positive and negative control, the dephosphorylated RNA was treated with the T4 polynucleotide kinase (PNK, NEB) (for 5′ phosphorylation of all RNA fragments) or was performed without adding the enzyme. 5′ RNA adaptor ligation was carried out by using the TruSeq Small RNA Sample Preparation Kit (Illumina). Reverse transcription was performed with SuperScript III enzyme (Invitrogen) and Illumina 3′ Adaptor Rev-Comp Random Hexamers (RC3N6). The RNA was size selected on TBE-Urea 10% PAGE gel and PCR amplification was carried out by using the TruSeq Small RNA Sample Preparation Kit (Illumina).

ART-seq library preparation. Ribosome profiling was performed using the ARTseq/TruSeq Ribo Profile (Illumina), with minor changes to the manufacturer protocol. In brief, around 3×10^7 cells were treated with 0.1 μg μl^{-1} final cycloheximide for 5 min at 37 °C. Cells were then washed twice and harvested with ice-cold PBS (supplemented with 0.1 μg μl^{-1} final cycloheximide). Cells were lysed in 1 ml of mammalian lysis buffer (supplemented with 0.5% final concentration of NP-40) at 4 °C for 10 min on a rotator. The lysate was then treated with 50 U of ART-seq nuclease for 45 min at 25 °C, with moderate shaking. 400 μl of the digested lysate were then layered on the top of a 2.5 ml sucrose cushion, and centrifuged at 265,000*g* for 5 h at 4 °C. After completely removing the supernatant, the pellet was resuspended in 100 μl nuclease-free water, and purified on RNA Clean & Concentrator-5 columns (Zymo Research). 5 μg of the recovered monosomal RNA was then subjected to two consecutive rounds of rRNA depletion using the Ribo-Zero Gold Kit (Human/Mouse/Rat, Epicentre), and then run on a 10% TBE-Urea PAGE gel for 25 min at 200 V. A gel slice corresponding to 28–30 nt was then cut, crushed, and RNA was recovered by passive diffusion at 4 °C for 16 h. The eluted RNA fragments were then end-repaired, ligated to the 3′ adaptor, and reverse-transcribed. The cDNA was run on 10% TBE-Urea PAGE gel for 30 min at 180 V, and a gel slice corresponding to fragments of approximately 70–80 nt was cut, crushed, and cDNA was recovered by passive diffusion at 37 °C for 16 h with vigorous shaking. The eluted cDNA was then subjected to circularization, and the final library was obtained by ten cycles of PCR. The final library was inspected on the Fragment Analyzer (Advanced Analytical), revealing a single sharp peak around 150 bp.

Reads mapping and data analysis. Samples were sequenced on the HiScanSQ or Next500 platforms (Illumina). All of the analysed datasets were mapped to a recently published variant of the mm9 genome assembly that includes single-nucleotide variants from E14 ES cells[45]. Prior to mapping, sequencing reads were trimmed on the basis of low-quality scores and clipped from the adaptor sequence by using FASTX toolkit (http://hannonlab.cshl.edu/fastx_toolkit/). For RNA-seq data analysis, reads were mapped using TopHat v2.0.6 (ref. 46) and mRNA quantification was performed using Cuffdiff v2.0.2 (ref. 47). For ChIP-seq data analysis, reads were mapped Bowtie version 0.12.7 (ref. 48), reporting only unique hits with up to two mismatches (parameters: -m 1 -v 2). For bisulphite-seq data analysis, reads were mapped using BSMAP v2.74 (ref. 49). Unmapped reads from the first mapping round were trimmed by 10 nt at their 5′ end, and 15 nt at their 3′ end using fastx_trimmer tool from the FASTX toolkit, and subjected to a second round of mapping. Reads failing this second mapping round were mapped to the *Escherichia coli* strain K-12 substrain DH10B genome (NCBI accession: NC_010473), in order to estimate bisulphite conversion efficiency.

RNA-seq analysis. RNA-seq correlation analyses were performed by using Pearson correlation coefficient and by plotting RPKM value calculated on RefFlat gene annotation. Intragenic transcription initiation analysis was performed on a non-redundant gene annotation built starting from the RefFlat annotation, by keeping only the longest isoform for each gene, with at least 1 RPKM of expression and at least 5 exons. RPKM on each exon was calculated by counting reads falling in the exon (normalizing on the exon length in kb and on the total mapped reads of the experiment in millions) using custom script and then the ratio was calculated as the $\log_2$ fold-change of second, third and last exon RPKM over the first exon RPKM for each gene. For the ratio of intermediate to first exons, averages of the RPKM value of all the other exons (from fourth to penultimate) were used. Alternative promoter analysis was performed on a non-redundant gene annotation built starting from the RefFlat annotation by keeping only the genes that had at least two isoforms transcribed from known different promoters. RPKM of the first exon of the isoforms transcribed from alternative promoters was calculated with a custom script. The $\log_2$ ratio between the first exons transcribed from the first over the second promoter was plotted by using the heatscatter function (on R) and correlation was quantified with Pearson's coefficient. Alternative promoter analysis was calculated on the same reference as above. The $\log_2$ ratio was calculated as the RPKM value of the first exon transcribed from each class of different alternative promoters over the RPKM of the whole transcript, in order to normalize differentially expressed genes in wild-type and *Dnmt3b*$^{-/-}$ cells.

DECAP-seq analysis. For DECAP-seq only intragenic mapped reads were used for further analysis. We used a RefSeq-based genic reference containing only the annotated longest isoforms and deprived from all the genes overlapping other genes or ncRNAs on the same strand. Since DECAP-seq is a technique capable of single-base resolution and the first base of the sequenced reads corresponds to the base having the cap signal, only the first position of the mapped read was used to calculate a count per million of mapped reads (RPM). All the analyses were performed on the genes belonging to the third or fourth quartiles of expression. Venn diagram overlap is calculated at single-base resolution. Logo analysis of the sequence enrichment was performed by using WebLogo (http://weblogo.berkeley.edu/). Motif discovery was performed by using HOMER Motif Analysis (http://homer.salk.edu/homer/motif/).

CAPIP-seq analysis. For CAPIP-seq only intragenic mapped reads were used for further analysis. RPKM of each genomic feature were calculated as described above by using custom script. Enrichment was calculated as the $\log_2$ fold change of RPKM value from CAP immunoprecipitated samples over the RPKM from input samples for each genomic feature. As for DECAP-seq, the intragenic CAPIP-seq signal ratio between wild-type and *Dnmt3b*$^{-/-}$ cells was calculated as the fold change of the intragenic enrichment (from 2 kb downstream TSS to TES) in wild-type over *Dnmt3b*$^{-/-}$ cells. The ratio gene-body to TSS was defined as the $\log_2$ fold change of gene-body enrichment (derived from intronic and intermediate exonic regions) over the enrichment calculated on the first 200 nt of the transcripts. All the analyses were performed on genes belonging to the third or fourth quartiles of expression.

Half-life analysis. Poly(A)$^+$ enriched RNA-seq analyses were performed from RNA derived from DRB-treated wild-type and *Dnmt3b*$^{-/-}$ ES cells. For half-life calculation, gene quantifications performed with CuffDiff (see above) were normalized on the average of the top ten genes showing less degradation rate following DRB treatment having at least 10 RPKM in ES cells. Degradation rate has been defined as the ratio of RPKM value of the sample at time 0 h of DRB treatment over the average RPKM value of the samples treated for 3, 6 and 12 h with DRB. The top ten genes are *Tmsb10*, *Mt1*, *Mt2*, *Rps14*, *Rplp2*, *4930412F15Rik*, *Rpl38*, *Rplp1*, *Tomm7* and *Cox6a1*. Only genes with a RPKM > 1 were used for further analysis and a constant of 0.1 pseudo-RPKM was introduced to reduce sampling noise. Half-life ($t_{1/2}$) was calculated by using the following formula[50]:

$$t_{1/2} = \frac{\ln [2]}{k_{\text{decay}}}$$

where k_{decay} is the decay rate constant obtained by fitting data (gene RPKM value for each time point) with an exponential function. Half-life on introns was measured as calculated for mature mRNAs, but gene quantification (RPKM) was performed counting the reads on introns and normalizing for intron length (kb) and for the number of total intragenic mapped reads (millions). For introns and exons quantification, reads were treated as above (see RNA-seq analysis).

Ribosome profiling analysis (ART-seq). Analysis of ART-seq experiments were performed as previously described[31]. Differently from the other sequencing data, for ribosome profiling, only adaptor containing reads were used in order to avoid total RNA contamination. Reads were clipped from adapters and mapped on

rRNAs and tRNAs. Only reads not mapping on rRNA/tRNA genes were used for downstream analysis. Quantification (RPKM) of the reads derived from different transcript parts or genomic features was performed as described above.

ChIP-seq and WGBS analysis. Following mapping, reads with the same start mapping coordinates were collapsed using custom Perl scripts, and peak calling was performed using MACS version 1.4.1 (ref. 51).

ChIP-seq signal $\log_2$ enrichment was calculated as previously described[10], with some modifications. In brief, the mouse genome was partitioned into 500-bp bins. Bins overlapping with satellite repeats and with an insufficient coverage in WGBS (less than 50% of all CpGs covered at least 10×) were removed resulting in 2,708,724 bins. Signal enrichment was calculated as the $\log_2$ of ChIP-seq over input RPKM. These whole-genome $\log_2$ enrichment values were used for clustering, correlation, box plot and scatter plot analysis by using custom scripts. For genomic binning by H3K36me3, the above bins were divided in ten equal-size groups rank-ordered by their $\log_2$ enrichment for H3K36me3.

Heat map representations of ChIP-seq peaks and plots were performed with respect to annotated RefSeq genes, sorted by their expression level, according to RNA-seq data. Plots of Dnmt3b and H3K36me3 distribution on genes clustered in quartiles of expression revealed an almost identical distribution for both features.

For the analysis of Dnmt3b intragenic binding in Setd2 knockdown ES cells and Dnmt3b-re-expressing *Dnmt3b*$^{-/-}$ ES cells, a non-redundant gene annotation was built starting from the RefFlat annotation, by keeping only the longest isoform for each gene. After calling H3K36me3 peaks in wild-type ES cells using MACS 1.4.1 (parameters: -p 1e-8 –nolambda), the genes from the RefFlat annotation that overlap an H3K36me3 peak were marked as H3K36me3-positive, while genes lacking any overlap were marked as H3K36me3-negative. For each gene in the two datasets, the normalized Dnmt3b signal (RPKM) in control and treated ES cells was calculated as:

$$\mathrm{RPKM} = \frac{10^9 \times n}{(\mathrm{TES} - \mathrm{TSS}) \times N}$$

where n is the number of Dnmt3b reads overlapping a gene's coordinates, TSS and TES are respectively the start and end coordinate of the gene annotation, and N is the total number of mapped reads in the ChIP-seq experiment. P values were calculated using a one-tailed paired Wilcoxon rank-sum test.

Methylation calling was performed using the methratio.py script provided with the BSMAP tool and comparative analyses were performed by using only CpG covered at least 5× in both wild-type and *Dnmt3b*$^{-/-}$ cells.

Heat maps and comparative analysis were performed using custom Perl scripts. Datasets used for comparative analysis were obtained from Gene Expression Omnibus by downloading the following datasets: GSE12241, GSE11172, GSE31039, GSE44642, GSE44566, GSE55660, GSE57413, GSE44566.

Antibodies. Antibodies were purchased from Abcam (anti-Dnmt3b; anti-H3K36me3; anti-single-strand DNA; anti-H3 pan; anti-Tbp; anti-TIIb), from Imgenex (anti-Dnmt3a; anti-Dnmt3b; anti-Dnmt1), from Diagenode (anti-5-methylcytidine), from Millipore (anti-H3K27me3; anti-m3G-cap, anti-m7G-cap; anti-Elk1), from Upstate (anti-H3K4me3), from Covance (anti-Pol II-phospho-Ser5), from SantaCruz (anti-pan Pol II, anti-Sp1; anti-Elf1), from Upstate (anti-H3K4me3; anti-H3ac). Anti-Dnmt3l was provided by S. Yamanaka.

Data availability. The raw data that support the findings of this study have been deposited at Gene Expression Omnibus under the accession code GSE72856.

41. Neri, F. *et al.* Genome-wide analysis identifies a functional association of Tet1 and Polycomb repressive complex 2 in mouse embryonic stem cells. *Genome Biol.* **14,** R91 (2013).
42. Mikkelsen, T. S. *et al.* Genome-wide maps of chromatin state in pluripotent and lineage-committed cells. *Nature* **448,** 553–560 (2007).
43. Incarnato, D., Neri, F., Diamanti, D. & Oliviero, S. MREdictor: a two-step dynamic interaction model that accounts for mRNA accessibility and Pumilio binding accurately predicts microRNA targets. *Nucleic Acids Res.* **41,** 8421–8433 (2013).
44. Incarnato, D., Neri, F., Anselmi, F. & Oliviero, S. Genome-wide profiling of mouse RNA secondary structures reveals key features of the mammalian transcriptome. *Genome Biol.* **15,** 491 (2014).
45. Incarnato, D., Krepelova, A. & Neri, F. High-throughput single nucleotide variant discovery in E14 mouse embryonic stem cells provides a new reference genome assembly. *Genomics* **104,** 121–127 (2014).
46. Kim, D. *et al.* TopHat2: accurate alignment of transcriptomes in the presence of insertions, deletions and gene fusions. *Genome Biol.* **14,** R36 (2013).
47. Trapnell, C. *et al.* Differential analysis of gene regulation at transcript resolution with RNA-seq. *Nat. Biotechnol.* **31,** 46–53 (2013).
48. Langmead, B., Trapnell, C., Pop, M. & Salzberg, S. L. Ultrafast and memory-efficient alignment of short DNA sequences to the human genome. *Genome Biol.* **10,** R25 (2009).
49. Xi, Y. & Li, W. BSMAP: whole genome bisulfite sequence MAPping program. *BMC Bioinformatics* **10,** 232 (2009).
50. Chen, C.-Y. A., Ezzeddine, N. & Shyu, A.-B. Messenger RNA half-life measurements in mammalian cells. *Methods Enzymol.* **448,** 335–357 (2008).
51. Zhang, Y. *et al.* Model-based analysis of ChIP-seq (MACS). *Genome Biol.* **9,** R137 (2008).
52. Li, J. Y. *et al.* Synergistic function of DNA methyltransferases Dnmt3a and Dnmt3b in the methylation of Oct4 and Nanog. *Mol. Cell. Biol.* **27,** 8748–8759 (2007).
53. Core, L. J., Waterfall, J. J. & Lis, J. T. Nascent RNA sequencing reveals widespread pausing and divergent initiation at human promoters. *Science* **322,** 1845–1848 (2008).
54. Sharova, L. V. *et al.* Database for mRNA half-life of 19 977 genes obtained by DNA microarray analysis of pluripotent and differentiating mouse embryonic stem cells. *DNA Res.* **16,** 45–58 (2009).
55. Schwanhäusser, B. *et al.* Global quantification of mammalian gene expression control. *Nature* **473,** 337–342 (2011).

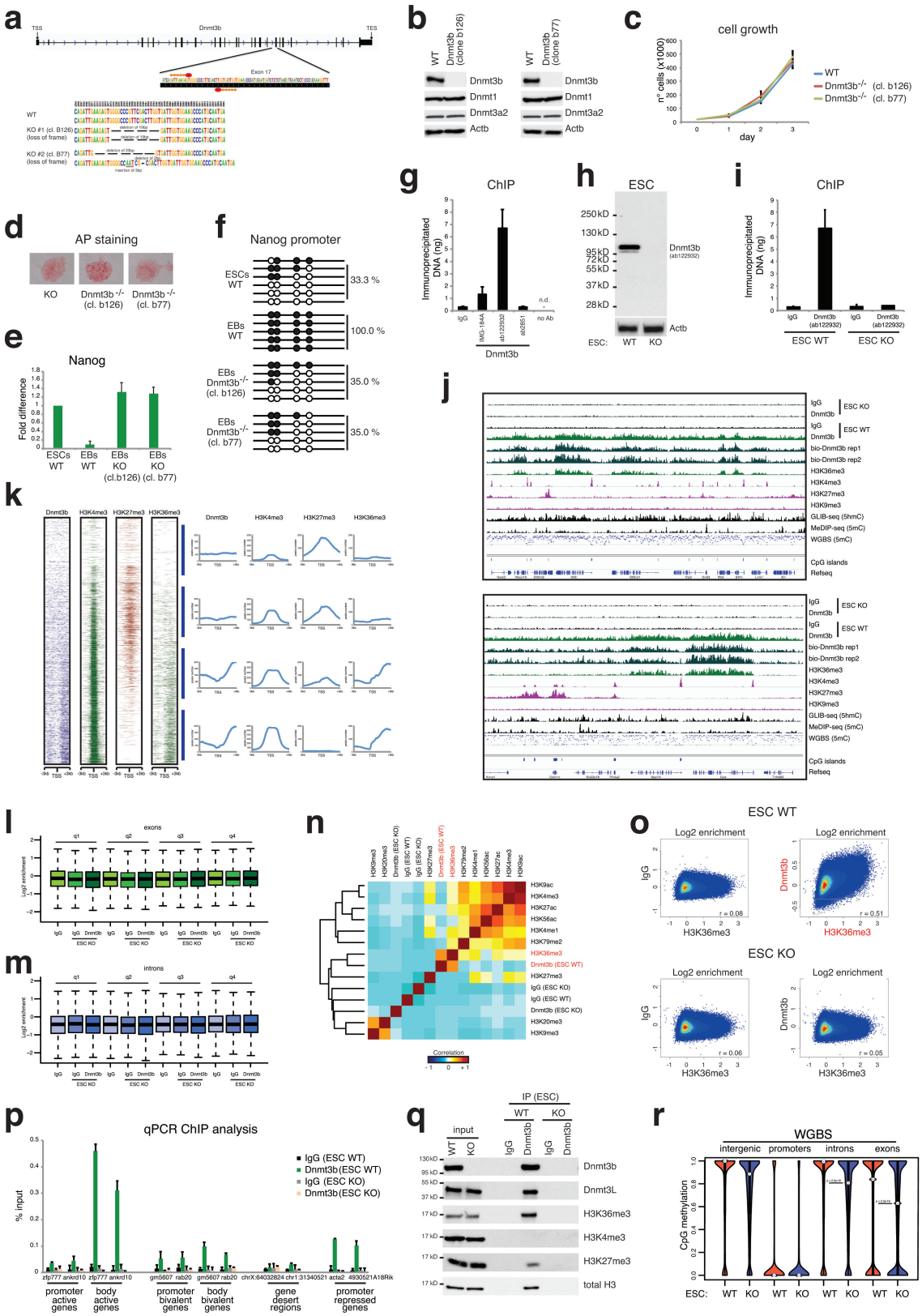

Extended Data Figure 1 | See next page for caption.

Extended Data Figure 1 | Generation of *Dnmt3b*$^{-/-}$ and mapping of the endogenous Dnmt3b in ES cells. *Dnmt3b*$^{-/-}$ ES cell clones (B126 and B77) showed normal cell growth and alkaline phosphatase (AP) staining as well as impaired silencing, by promoter DNA methylation of Nanog expression during the differentiation into embryonic bodies (EBs) with respect to the wild-type cell line, indicating the bona fide nature of the transgenic cell lines. **a**, Schematic of the region of the *Dnmt3b* gene targeted by TALEN zinc-fingers, and representative sequences on the two alleles of two *Dnmt3b*$^{-/-}$ clones, compared to wild-type (KO #1 = B77; KO #2 = B126). **b**, Western blot analysis of Dnmt3b protein in the two *Dnmt3b*$^{-/-}$ clones compared to wild-type. Dnmt1 and Dnmt3a2 levels are not affected by loss of Dnmt3b. Actin is used as loading control. Notably, the mRNA level (data not shown) of the Dnmt3b gene is also almost completely lost in *Dnmt3b*$^{-/-}$ cells. **c**, Growth curve of wild-type and *Dnmt3b*$^{-/-}$ ES cells over 3 days. **d**, Alkaline phosphatase staining of wild-type and *Dnmt3b*$^{-/-}$ ES cell colonies. **e**, RT–qPCR of Nanog levels in embryoid bodies derived from *Dnmt3b*$^{-/-}$ clones, compared to wild-type ES cells, and embryoid bodies. Error bars represent the standard deviation of at least three independent experiments. **f**, Sanger sequencing of bisulphite-treated genomic DNA from wild-type ES cells and embryoid bodies, and *Dnmt3b*$^{-/-}$ ES-cell-derived embryoid bodies, at the region of the Nanog promoter previously shown to be target of Dnmt3b-mediated methylation upon differentiation[52]. **g**, Histogram showing the quantity of the DNA recovered in ChIP experiments performed with different antibodies directed against Dnmt3b protein. **h**, Western blot analysis of Dnmt3b protein in wild-type and *Dnmt3b*$^{-/-}$ ES cells. Actin was used as a loading control. **i**, Histogram showing the quantity (ng) of the DNA recovered in ChIP experiments performed with anti-Dnmt3b antibody (Ab122932) in wild-type and *Dnmt3b*$^{-/-}$ ES cells. **j**, Genomic views of the mapped reads from different ChIP-seq datasets in ES cells. IgG and Dnmt3b ChIP-seq and WGBS are from the present work, bio-Dnmt3b from GSE57413, MeDIP-seq from GSE44644, GLIB-seq from GSE44566, histone modifications from GSE12241. **k**, Left, heat map representations of Dnmt3b binding and relevant histone modifications on a window of ±3 kb centred on the TSS of RefSeq genes, sorted by their expression level, according to RNA-seq data. Right, plots of Dnmt3b binding and relevant histone modifications on a window of ±3 kb centred on the TSS of RefSeq genes, clustered in the four quartiles of expression (q4 = upper quartile, the most expressed genes). **l**, **m**, Binding enrichment of IgG (in wild-type ES cells) as well as IgG and Dnmt3b (in *Dnmt3b*$^{-/-}$ ES cells) on the exons or introns partitioned in quartiles on the basis of the expression of the related gene. These figures represent control experiments for the Fig. 1b. **n**, Hierarchical clustering of pairwise Pearson correlation of Dnmt3b, and third-party ChIP-seq datasets in ES cells, reveals a strong genome-wide association of Dnmt3b with H3K36me3 histone marks. **o**, Scatter plots comparing intragenic H3K36me3 and IgG/Dnmt3b enrichments ($\log_2$) in wild-type and *Dnmt3b*$^{-/-}$ cells. r, Pearson correlation. **p**, qPCR of ChIP analysis of Dnmt3b on the indicated regions. A specific enrichment can be observed on gene body of active genes. Error bars represent the standard deviation of at least three independent experiments. Primers used are reported in Supplementary Table 1. **q**, Immunoprecipitation experiment (using a different antibody for Dnmt3b, Ab2851) in ES cells reveals the interaction of Dnmt3b with H3K36me3, but not H3K4me3, in agreement with ChIP-seq data. **r**, Violin plots of the methylation level of all CpGs in both wild-type and *Dnmt3b*$^{-/-}$ ES cells as determined by WGBS on the indicated genomic features. *P* values calculated with Wilcoxon rank-sum test.

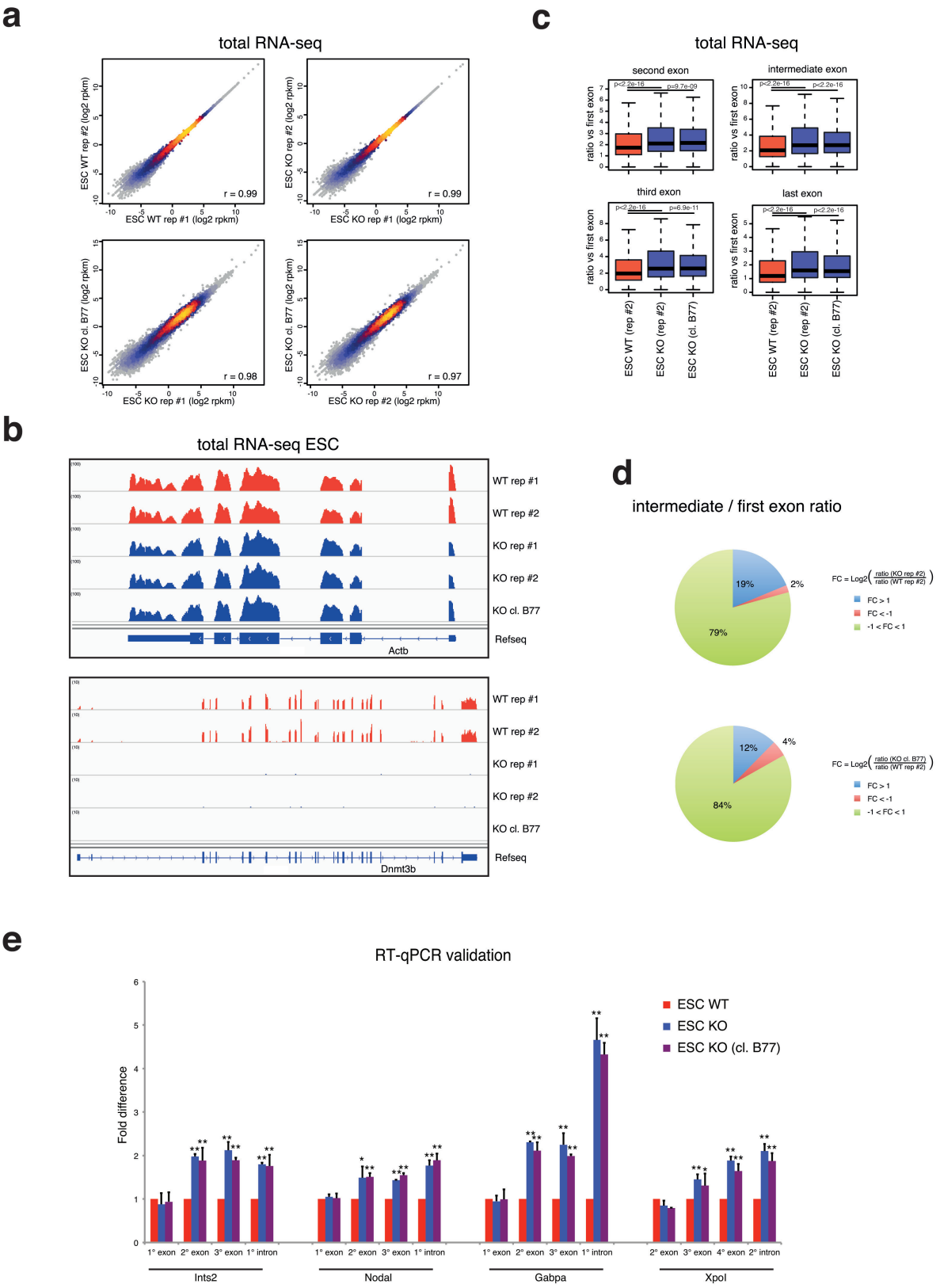

Extended Data Figure 2 | Dnmt3b loss increases intragenic RNA transcription initiation. a, Scatter plots of the $\log_2$ RPKM gene values in the indicated samples. **b**, Genomic views of the RNA-seq mapped reads from the indicated samples. **c**, Box plots of the ratio between normalized RNA-seq read counts (RPKM) for the second and the first exon (top left), the third and the first exon (bottom left), the average of the intermediate exons (from the fourth to penultimate) and the first exon (top right), the last and the first exon (bottom right), in wild-type (rep #2) and *Dnmt3b*$^{-/-}$ (rep #2 and clone B77) ES cells. *P* values calculated with Wilcoxon rank-sum test. **d**, Pie charts showing the percentage of transcripts with $\log_2$ fold change $\geq 1, \leq -1$ or between -1 and 1. **e**, RT–qPCR analysis of Ints2, Nodal, Gabpa and XpoI transcripts by using primers targeting different exons to discriminate different isoforms in wild-type, *Dnmt3b*$^{-/-}$ (cl. B126) and *Dnmt3b*$^{-/-}$ (cl. B77) ES cells. All the PCR were normalized to β-actin and on the wild-type condition. Error bars represent the standard deviation of at least three independent experiments. *P* values calculated against wild type condition for each experiment by using *t*-test. $^{**}P < 0.001$, $^{*}P < 0.01$. Primers used are reported in Supplementary Table 1.

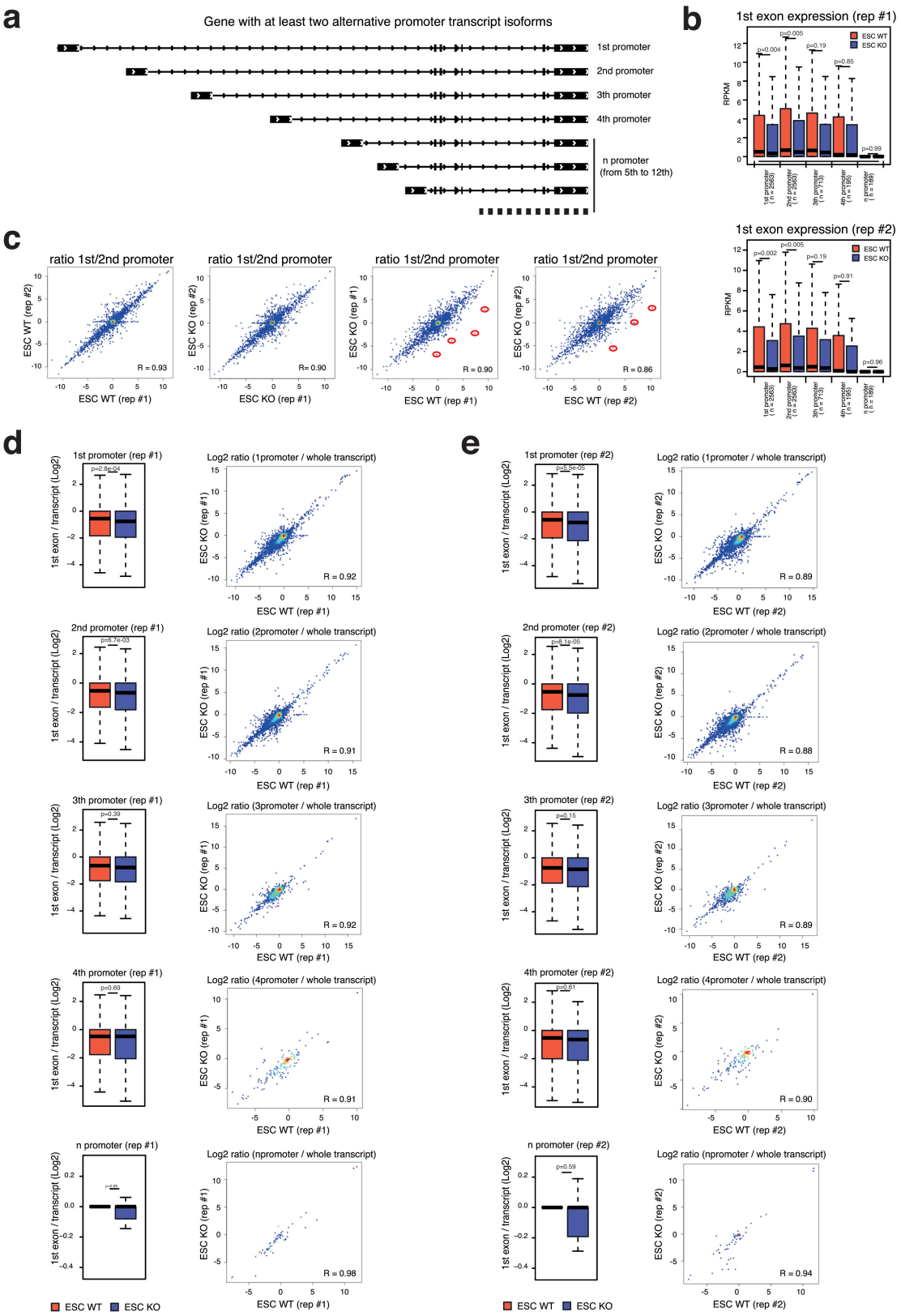

Extended Data Figure 3 | See next page for caption.

Extended Data Figure 3 | Dnmt3b loss does not extensively affect alternative promoter activation. We investigate the activation or repression of alternative promoters on the subset of genes showing at least two annotated alternative promoters. On these genes, we measured the RPKM value of the first exon of all the isoforms transcribed from each of the alternative promoters in wild-type or *Dnmt3b*$^{-/-}$ cells. We observed that the *Dnmt3b*$^{-/-}$ cells showed a general trend to exhibit genes with the first exon less expressed independently from the isoform, thus suggesting a non-global general activation of intragenic promoters. Analysis of the ratio of the expression between the first promoter and the second downstream promoter identified four genes (on a total of 2,563 genes) with a reactivation of the intragenic promoter in *Dnmt3b*$^{-/-}$ cells. **a**, Schematic of the gene dataset used for alternative promoter analysis. The dataset is composed of total 2,563 genes showing at least two annotated alternative promoters, including 713 genes having at least three, 195 genes at least four and another 189 genes with multiple alternative promoters (from at least 5 to a maximum of 12). **b**, RPKM value of the first exon of all the isoforms transcribed from the alternative promoters in wild-type or *Dnmt3b*$^{-/-}$ ES cells. *Dnmt3b*$^{-/-}$ cells showed a general trend to have genes with the first exon less expressed independently from the isoform, and none of putative intragenic promoters (from the second to the twelfth) showed general activation. **c**, Analysis of the ratio of the expression of the first promoter over the second downstream promoter displayed high correlation between replicates and wild-type or *Dnmt3b*$^{-/-}$ ES cells. Only four genes (of a total of 2,563 genes) showed a reactivation of the intragenic promoter in *Dnmt3b*$^{-/-}$ ES cells. Further analysis of the ratio between RPKM of the first exon and of the whole transcript for each class of alternative-promoter-transcribed genes did not show any evidence for possible reactivation of any class of transcript isoforms derived from intragenic promoters. **d**, **e**, Analysis of the ratio of the RPKM value of the first exon over the whole transcript for each class of alternative promoters transcribed genes showed high correlation between wild-type and *Dnmt3b*$^{-/-}$ ES cells and did not reveal evidence for possible reactivation of any class of transcript isoforms derived from intragenic promoters.

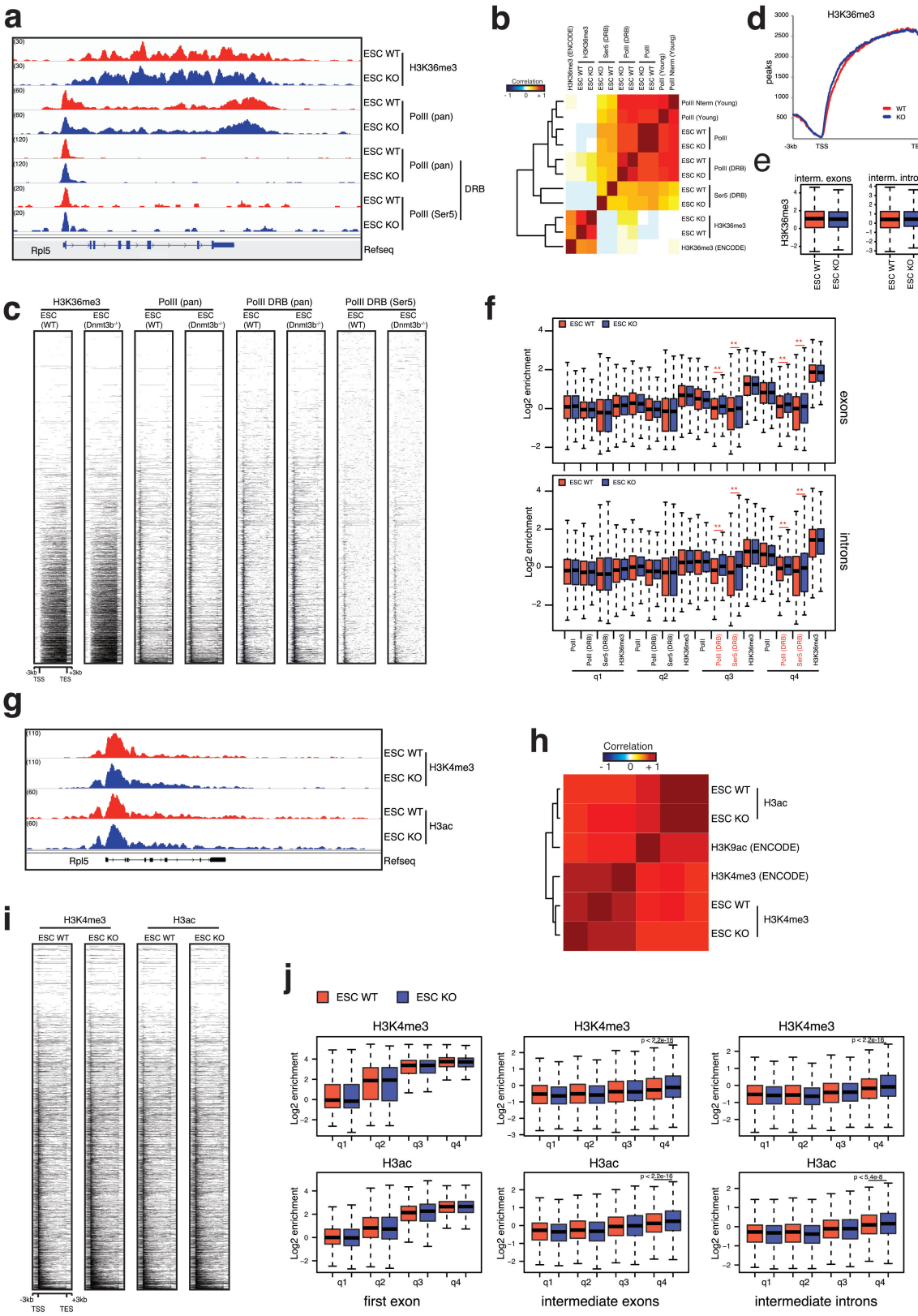

Extended Data Figure 4 | See next page for caption.

Extended Data Figure 4 | Dnmt3b loss does not globally affect elongating Pol II or H3K36me3 deposition on the gene bodies, but increases intragenic Pol II spurious entry. a, Genomic views of the mapped reads from the indicated different ChIP-seq data sets in wild-type and *Dnmt3b*$^{-/-}$ ES cells normally cultured or treated with the Pol II elongation inhibitor DRB. **b**, Hierarchical clustering of pairwise Pearson correlation of ChIP-seq experiments performed in this work, and third-party ChIP-seq datasets in ES cells. **c**, Heat map representations of the indicated ChIP-seq (in wild-type and *Dnmt3b*$^{-/-}$ ES cells) peaks with respect to annotated RefSeq genes, sorted by their expression level, according to RNA-seq data. Each gene was extended by 3 kb upstream of its TSS, and downstream of its TES. **d**, Plots of the H3K36me3 distribution in wild-type and *Dnmt3b*$^{-/-}$ ES cells. **e**, Binding enrichment of H3K36me3 on intermediate exons and introns in wild-type and *Dnmt3b*$^{-/-}$ ES cells. **f**, Binding enrichment of the indicated ChIP-seq experiments in wild-type and *Dnmt3b*$^{-/-}$ ES cells treated (or not) with DRB on the intermediate exons and introns subdivided into quartiles on the basis of expression level. This result demonstrated that only non-elongating Pol II is enriched on the bodies of the most expressed genes (q3 and q4) in *Dnmt3b*$^{-/-}$ ES cells. *P* values calculated with Wilcoxon rank-sum test; $^{**}P < 2.2 \times 10^{-16}$. **g**, Genomic views of the mapped reads from the ChIP-seq analyses for H3K4me3 and H3ac in wild-type and *Dnmt3b*$^{-/-}$ ES cells. **h**, Hierarchical clustering of pairwise Pearson correlation of ChIP-seq experiments performed in this work, compared with ENCODE ChIP-seq datasets. **i**, Heat map representations of the indicated ChIP-seq (in wild-type and *Dnmt3b*$^{-/-}$ ES cells) peaks with respect to annotated RefSeq genes, sorted by their expression level, according to RNA-seq data. Each gene was extended by 3 kb upstream of its TSS, and downstream of its TES. **j**, Binding enrichment of the indicated ChIP-seq experiments in wild-type and *Dnmt3b*$^{-/-}$ ES cells on the first exons, intermediate exons and introns subdivided into quartiles on the basis of expression level. This result demonstrates that H3K4me3 and H3ac distribution are enriched on the intermediate exons and introns of the most expressed genes of the *Dnmt3b*$^{-/-}$ ES cells. *P* values calculated with Wilcoxon rank-sum test.

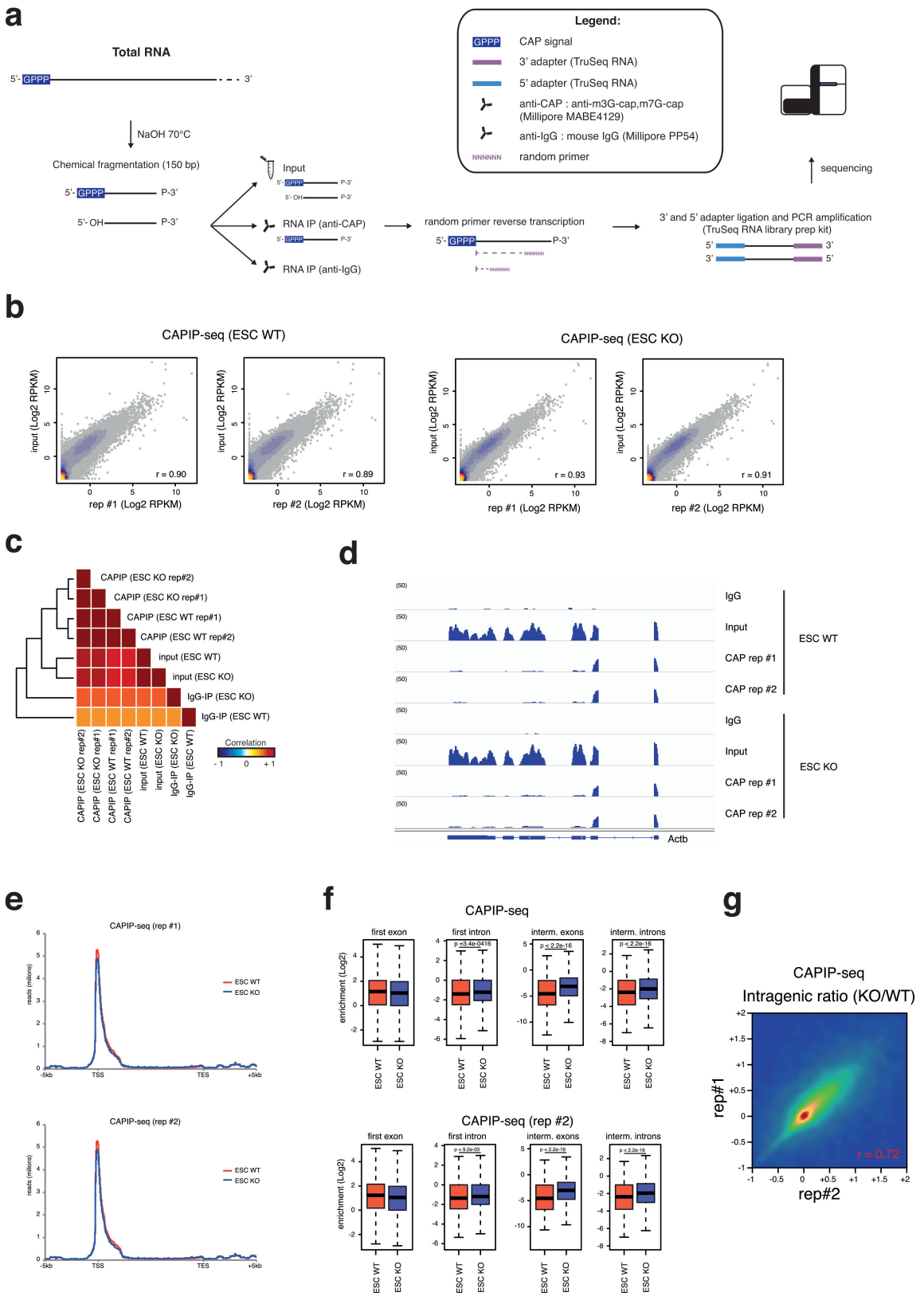

Extended Data Figure 5 | See next page for caption.

Extended Data Figure 5 | CAPIP-seq enrichment of the 5′ of the RNAs shows that Dnmt3b loss increases intragenic spurious transcription initiation. a, Schematic view of the CAPIP-seq protocol used. Total RNA is chemically fragmented and then subjected to immunoprecipitation by using a specific anti-CAP antibody or a control anti-IgG antibody. Eluted RNA (as well as one-tenth of the starting material for input) is subjected to random primer reverse-transcription. The library is then completed, starting from second strand generation. **b**, Scatter plots of the $\log_2$ RPKM of CAPIP-seq data (anti-CAP antibody) and input in wild-type and *Dnmt3b*$^{-/-}$ ES cells. **c**, Hierarchical clustering of pairwise Pearson correlation of CAPIP-seq-related sequencings in wild-type and *Dnmt3b*$^{-/-}$ ES cells. **d**, Genomic views of the total mapped reads from the indicated CAPIP-seq related sequencings. Enrichment of the CAP signal is present on the 5′ of the RNA as a peak of about 150 bp broader with respect to the signal obtained by performing DECAP-seq. **e**, Plots of the CAPIP-seq mapped reads distribution in wild-type and *Dnmt3b*$^{-/-}$ ES cells with respect to annotated RefSeq genes, extended by 5 kb upstream of its TSS, and downstream of its TES. **f**, Box plots of the $\log_2$ enrichment of the CAPIP-seq signal rep #2 (CAP immunoprecipitation signal over input in wild-type and *Dnmt3b*$^{-/-}$ ES cells on the indicated genic features). *P* values calculated with Wilcoxon rank-sum test. **g**. Further analysis showing the increase of CAP localization from intragenic regions of the RNA. Intragenic ratio is calculated as the $\log_2$ ratio of cap signal gene-body enrichment in *Dnmt3b*$^{-/-}$ versus wild-type cells. The correlation between the two replicates is shown.

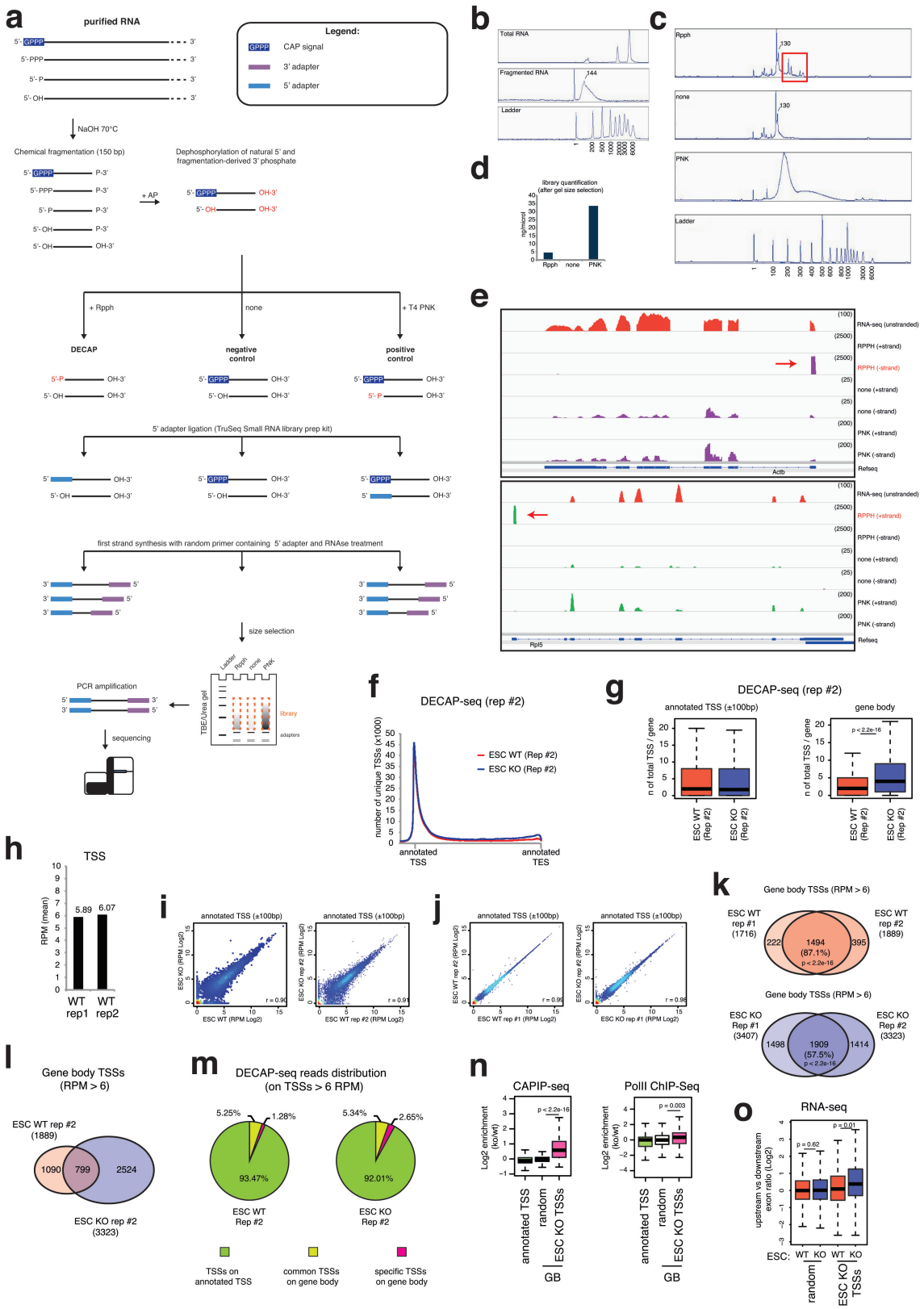

Extended Data Figure 6 | See next page for caption.

Extended Data Figure 6 | DECAP-seq method maps, at single-base resolution, TSSs on the gene body in ES cells. a, Schematic representation of the workflow of the DECAP-seq technique that is based on the RNA 5′ pyrophosphohydrolase (RppH) enzymatic activity that in Thermopol buffer is able to mediate decapping and pyrophosphate removal from the 5′ end of RNA to leave a 5′ monophosphate RNA (5′-P). 5′-P RNA is then used for selective adaptor ligation by T4 RNA ligase to the originally capped RNA fragments allowing single-base resolution mapping of the RNA capping sites. Treating sample in the same way, but without RppH enzyme generates a negative control (to detect technical background). Positive control is generated by treating sample with T4 polynucleotide kinase (PNK) for 5′ phosphorylation of all RNA fragments. This method represents an affordable alternative to the use of the tobacco acid pyrophosphatase (TAP) enzyme that has been used in several high-throughput techniques such as GRO-seq, CAP-seq, CIP-TAP[53] because the EpiCentre Technologies (to our knowledge, the only company producing commercial TAP) has discontinued TAP and all kits containing it. **b**, Total RNA fragmentation was verified by using Fragment Analyzer (Advanced Analytical). **c**, Final DECAP-seq libraries were inspected on Fragment Analyzer before gel size selection. RppH-treated and untreated samples showed a double peak around 130 bp corresponding to the dimers of adaptor, but only the RppH-treated sample showed a higher enrichment (in the red box) corresponding to the decapped RNA fragments. The PNK-treated sample displayed a large peak around 200 bp. **d**, Final DECAP-seq libraries were quantified on Qubit (Invitrogen) after gel size selection and PCR enrichment. The library generated by treating RNA with RppH showed a fifty-fold higher concentration with respect to the library generated without RppH treatment (5 ng μl^{-1} versus 0.1 ng μl^{-1}). **e**, Genomic views of the total DECAP-seq mapped reads from the indicated treatment on a gene (*Actb*) on the Crick DNA strand (− strand) and a gene (*Rpl5*) on the Watson DNA strand (+ strand). A pronounced sharp peak (red arrow) is present on the TSS only on the respective gene strand, thus reflecting both the cap- and strand-specificity of the method. Unstranded RNA-seq is shown as reference example. **f**, Plot of total TSSs (identified by using DECAP-seq rep #2) distribution along genes in *Dnmt3b*$^{-/-}$ (blue line) compared with wild-type (red line) ES cells. **g**, Box plots showing the number of total TSSs per gene on RefSeq-annotated TSSs and on gene body in wild-type and *Dnmt3b*$^{-/-}$ ES cells. *P* values calculated with Wilcoxon rank-sum test. **h**, Histogram showing the average RPM of novel identified TSSs by DECAP-seq in both replicates of wild-type ES cells. **i**, **j**, Scatter plots of the $\log_2$ RPM values on canonical annotated TSSs (±100 bp) in both replicate of DECAP-seq samples in wild-type and *Dnmt3b*$^{-/-}$ ES cells. **k**, Venn diagrams of intragenic TSSs with a DECAP-seq signal RPM > 6 showing the single-base resolution overlap between the DECAP-seq experiment replicates. *P* values calculated with Hypergeometric Distribution test. **l**, Venn diagram of intragenic TSSs with a DECAP-seq signal RPM > 6 showing single-base resolution overlap between *Dnmt3b*$^{-/-}$ and wild-type ES cells (rep #2). **m**, Pie charts of the DECAP-seq read distribution on TSSs RPM > 6 in wild-type (left) and *Dnmt3b*$^{-/-}$ (right) cells (rep #2). In green are shown the novel TSSs that overlap with RefSeq-annotated TSSs. Yellow, all the common TSSs distributed on the gene body; pink, the sample-specific TSSs on the gene body. **n**, Box plot distribution of the enrichment of the CAPIP-seq and Pol II ChIP-seq signals calculated as the $\log_2$ ratio in *Dnmt3b*$^{-/-}$ versus wild-type cells on the novel identified TSSs and on an intragenic random dataset. Green, those overlapping with RefSeq-annotated TSSs; pink, those specifically found on the gene bodies of *Dnmt3b*$^{-/-}$ ES cells. *P* values calculated with Wilcoxon rank-sum test. **o**, Box plot distribution of the ratio between downstream and upstream exon expression levels with respect to the novel identified intragenic TSSs or an intragenic random dataset in *Dnmt3b*$^{-/-}$ cells. The exon expression levels were calculated by counting the reads from the RNA-seq experiments in *Dnmt3b*$^{-/-}$ or wild-type cells. *P* values calculated with Wilcoxon rank-sum test.

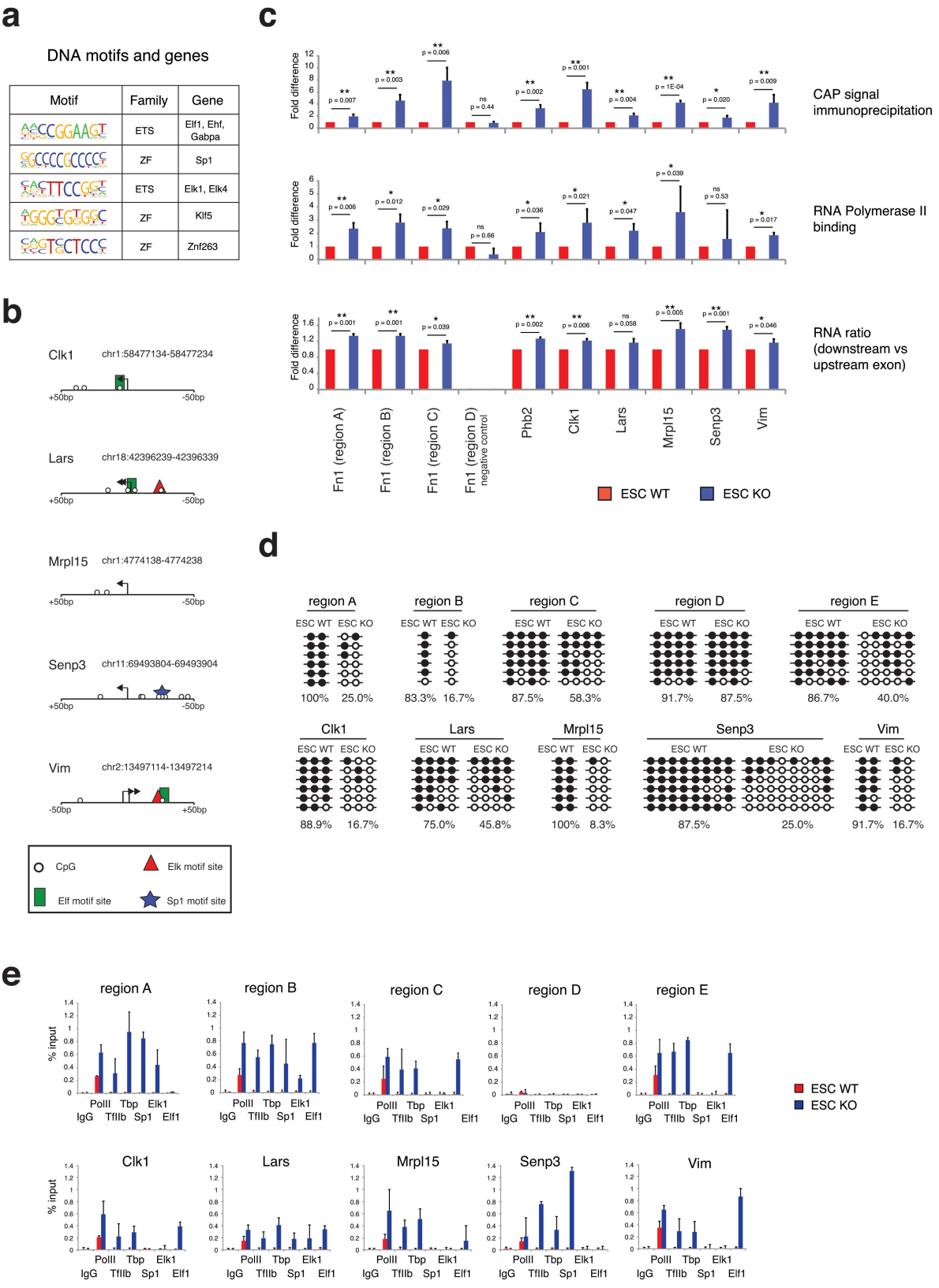

Extended Data Figure 7 | DECAP-seq maps the internal TSSs in *Dnmt3b*$^{-/-}$ ES cells revealing their correlation with the binding of methylation-sensitive transcription factors. a, Sequence binding motifs of the indicated transcription factors. **b**, Schematic representation of CpG localization and putative transcription factor binding elements on the regions (±50 bp) of some intragenic TSSs specific to *Dnmt3b*$^{-/-}$ ES cells. **c**, RT–qPCR analysis of CAPIP (top) and qPCR analysis of ChIP (middle) experiments on the indicated genomic regions in wild-type and *Dnmt3b*$^{-/-}$ ES cells. For CAPIP RT–qPCR the primers were designed downstream the novel identified TSSs. Bottom panel represents the fold difference of the ratio between downstream and upstream exon expression levels with respect to the novel identified intragenic TSSs. For TSSs falling on exons, the downstream or upstream part of the same exon was considered as downstream or upstream exon if longer than 200 bp. *P* value was calculated against the wild-type condition using a *t*-test; $^{**}P < 0.01$; $^{*}P < 0.05$; n.s., not significant. **d**, Sanger bisulphite sequencing of intragenic TSSs previously described in wild-type and *Dnmt3b*$^{-/-}$ ES cells. **e**, qPCR analysis of ChIP experiments on the indicated genomic regions.

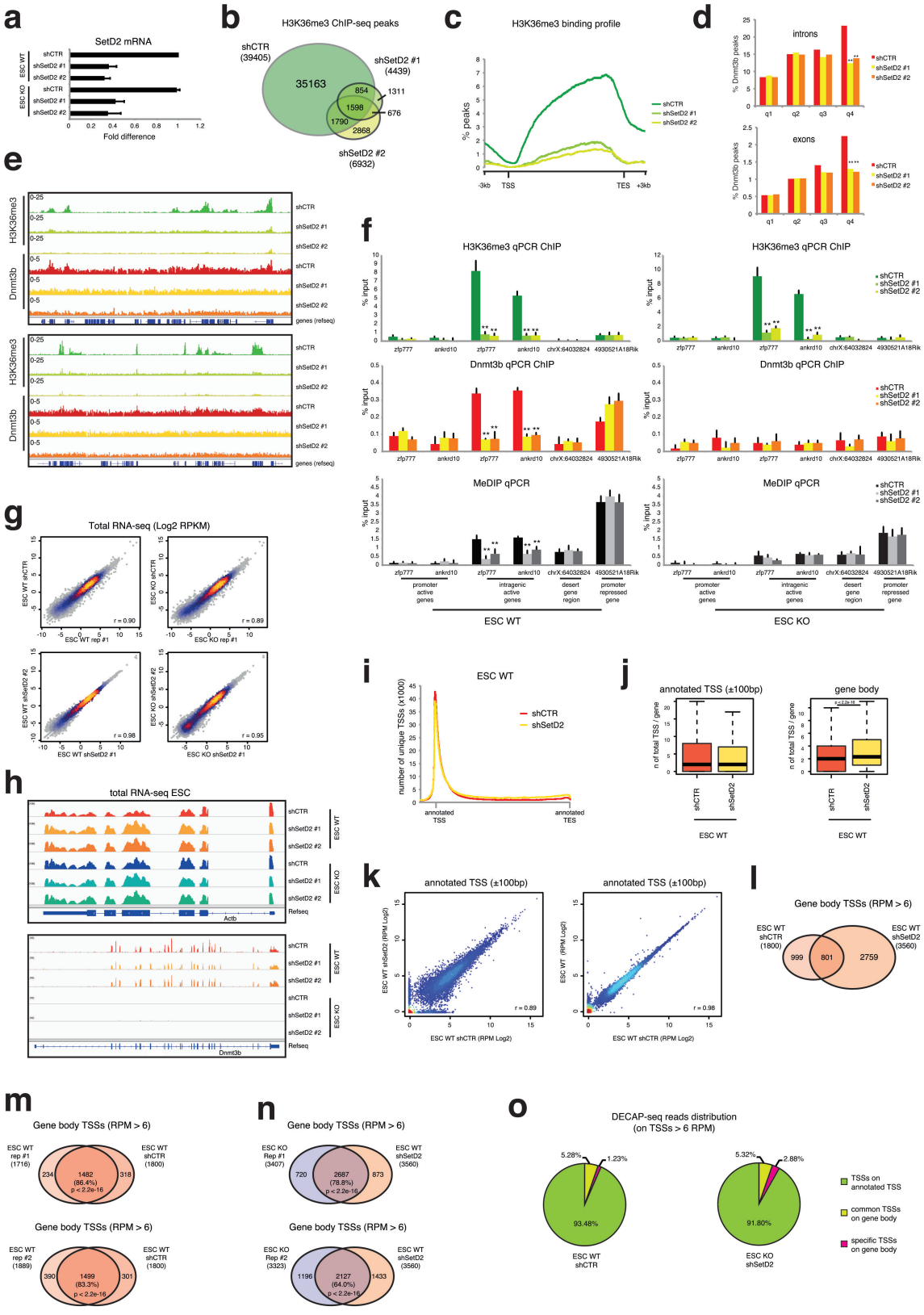

Extended Data Figure 8 | See next page for caption.

Extended Data Figure 8 | SetD2 knockdown reduces H3K36me3 marks, Dnmt3b binding, intragenic DNA methylation, and spurious TSSs on the gene bodies. a, RT–qPCR of SetD2 knockdown in wild-type and *Dnmt3b*$^{-/-}$ ES cells, using two independent shRNAs. Error bars represent the standard deviation of at least three independent experiments. **b**, Venn diagram showing the genome-wide number of H3K36me3 peaks in control and SetD2 knockdown ES cells. **c**, Plots of H3K36me3 distribution on genes in control and SetD2 knockdown cells show a decrease of H3K36me3 on the gene bodies of SetD2-silenced cells. **d**, Histograms of the percentage of Dnmt3b ChIP-seq peaks overlapping intronic and exonic regions of genes grouped into quartiles on the basis of expression in control or SetD2 knockdown cells. *P* value was calculated with a χ^2 test; $^{**}P < 0.001$. **e**, Genomic views of the mapped reads from H3K36me3 and Dnmt3b ChIP-seq datasets in control and two different SetD2 knockdowns ES cells. **f**, qPCR analysis of H3K36me3 and Dnmt3b ChIP experiments and MeDIP analysis in control and SetD2 knockdown cells for the indicated genomic regions. A specific loss of Dnmt3b and DNA methylation is observed only on the gene body of active genes. Error bars represent the standard deviation of at least three independent experiments. *P* value was calculated against the wild-type condition for each experiment with a *t*-test; $^{**}P < 0.001$. Primers used are reported in Supplementary Table 1. **g**, Scatter plots of the $\log_2$ RPKM gene values in the indicated samples. **h**, Genomic views of the RNA-seq-mapped reads from the indicated samples. **i**, Plot of total TSSs (identified by using DECAP-seq) distribution along genes in SetD2 knockdown (yellow line) compared with control knockdown (red line) ES cells. **j**, Box plots showing the number of total TSSs per gene on RefSeq-annotated TSSs and on gene bodies in control and SetD2 knockdown ES cells. *P* values calculated with Wilcoxon rank-sum test. **k**, Scatter plots of the $\log_2$ RPM values on canonical annotated TSSs ($\pm$100 bp) in control and SetD2 knockdown ES cells. **l**, Venn diagram of intragenic TSSs with a DECAP-seq signal RPM > 6 showing single-base resolution overlap between control and SetD2 knockdown ES cells. **m**, **n**, Venn diagrams of intragenic TSSs having DECAP-seq signal RPM > 6 showing single-base resolution overlap between the indicated samples. *P* values calculated with Hypergeometric Distribution test. **o**, Pie charts of the DECAP-seq read distribution on TSSs RPM > 6 in control knockdown (top) and SetD2 (bottom) ES cells. In green are the novel TSSs that overlap with RefSeq-annotated TSSs; in yellow, all the common TSSs distributed on gene bodies; and in pink, the sample-specific TSSs on gene bodies.

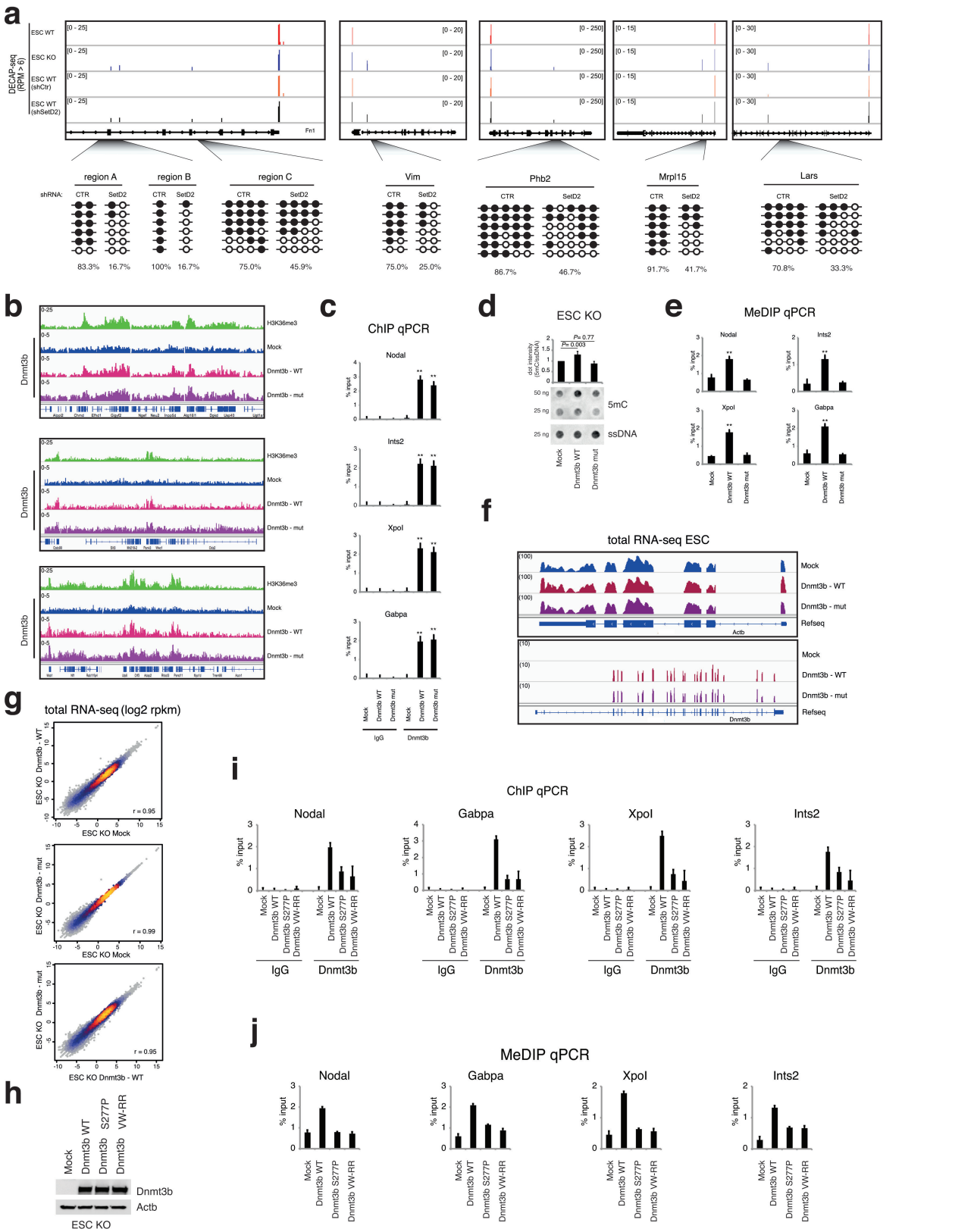

Extended Data Figure 9 | See next page for caption.

Extended Data Figure 9 | Internal transcription activation in *Dnmt3b*$^{-/-}$ ES cells show the same intragenic TSSs as in SetD2 knockdown cells. a, Genomic view of the indicated genes showing intragenic transcription initiation increase in *Dnmt3b*$^{-/-}$ and in shSetD2 wild-type cells. Below, Sanger bisulphite sequencing of shCTR (control) and shSetD2 wild-type ES cells on previously described intragenic TSSs. **b**, Genomic views of the mapped reads from H3K36me3 (in wild-type ES cells) and Dnmt3b ChIP-seq datasets (in mock or Dnmt3b-transfected *Dnmt3b*$^{-/-}$ ES cells). Both the wild-type and the catalytically inactive Dnmt3b(V725G) mutant showed intragenic binding enrichment. **c**, qPCR analysis of IgG and Dnmt3b ChIP experiments in mock or Dnmt3b (wild-type and V725G) transfected *Dnmt3b*$^{-/-}$ ES cells for the indicated intragenic regions. Error bars represent the standard deviation of at least three independent experiments. *P* value calculated against the mock condition using a *t*-test; $^{**}P < 0.001$. Primers used are reported in Supplementary Table 1. **d**, Dot-blot analysis of genomic DNA isolated from mock or Dnmt3b (wild-type and V725G) transfected *Dnmt3b*$^{-/-}$ ES cells. Dot intensity quantification from three biological replicates revealed that wild-type Dnmt3b (but not the V725G mutant) significantly ($P = 0.003$) increased global DNA 5mC. *P* value calculated against the mock condition using a *t*-test. **e**, qPCR analysis of MeDIP experiments in mock or Dnmt3b (wild-type and V725G) transfected *Dnmt3b*$^{-/-}$ ES cells for the indicated intragenic regions. A significant intragenic increase of DNA methylation is evident in wild-type Dnmt3b (but not mutant) transfected *Dnmt3b*$^{-/-}$ ES cells. Error bars represent the standard deviation of at least three independent experiments. *P* value calculated against the mock condition using a *t*-test; $^{**}P < 0.001$. Primers used are reported in Supplementary Table 1. **f**, Genomic views of the RNA-seq-mapped reads from the indicated samples. **g**, Scatter plots of the $\log_2$ RPKM gene values in the indicated samples. Of note, mock-treated ES cells showed higher correlation with Dnmt3b-mutant-transfected ES cells ($r = 0.99$) than with wild-type Dnmt3b-transfected ES cells ($r = 0.95$), suggesting that DNA methylation enzymatic activity is the major driver of the Dnmt3b-dependent transcriptome alterations. **h**, Western blot of *Dnmt3b*$^{-/-}$ ES cells transfected with mock, wild-type Dnmt3b, Dnmt3b(S277P) or Dnmt3b(VW-RR). β-Actin was used as protein loading control. **i**, **j**, qPCR analysis of ChIP and MeDIP experiments of the indicated regions in Dnmt3b mutant conditions. Specific impairment of Dnmt3b binding and DNA methylation is observed in both the mutants compared to rescue using the wild-type Dnmt3b enzyme. Error bars represent the standard deviation of at least three independent experiments. Primers used are reported in Supplementary Table 1.

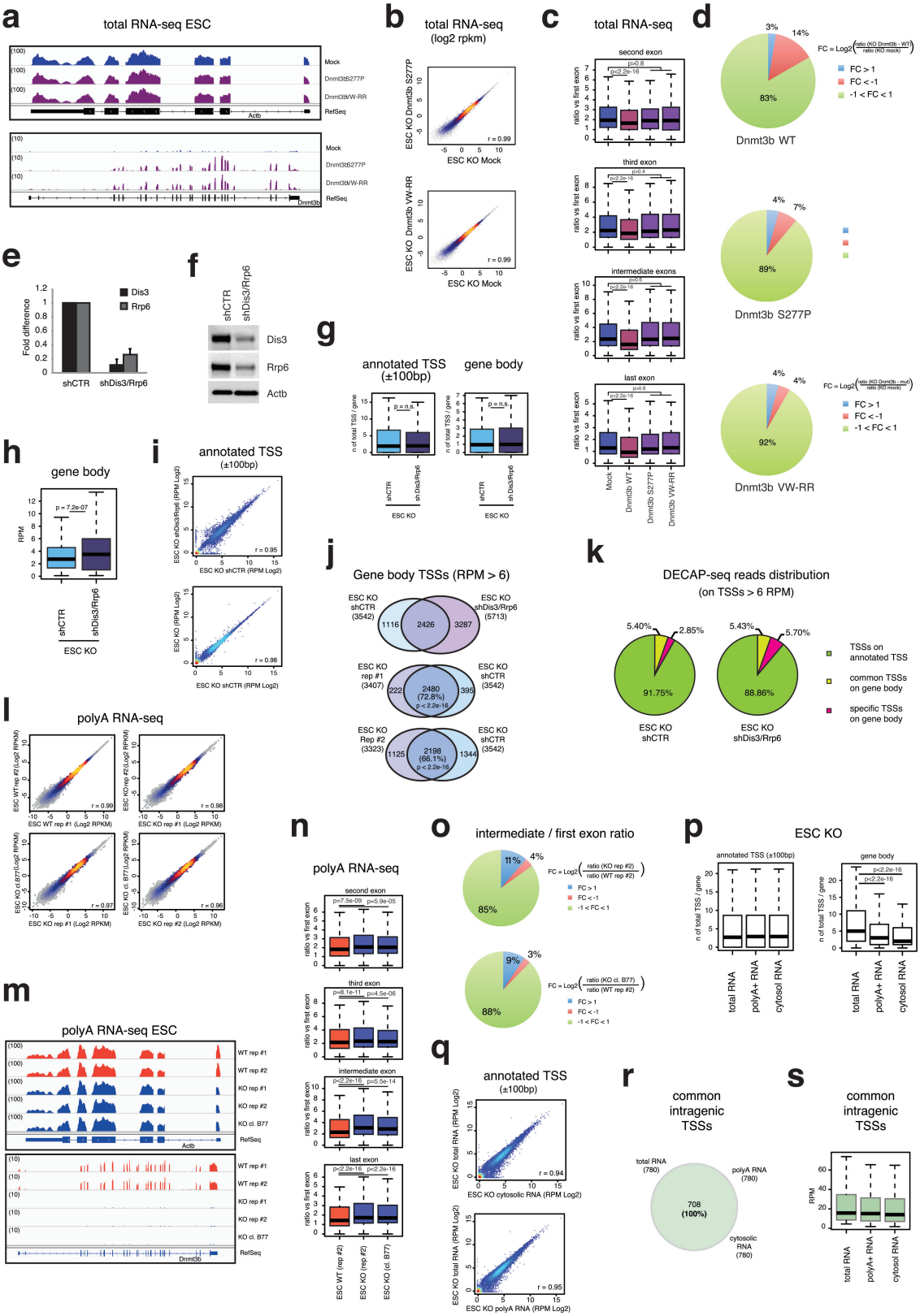

Extended Data Figure 10 | See next page for caption.

Extended Data Figure 10 | Cryptic RNA transcripts are degraded in part by the RNA exosome complex. a, RNA-seq profile of *Dnmt3b*$^{-/-}$ cells transfected with mock or Dnmt3b mutants. **b**, Scatter plots of the $\log_2$ RPKM gene values in the indicated samples. **c**, Box plot of the ratio between normalized RNA-seq read counts (RPKM) for the second, third, intermediate (average) and last exons to the first exon in *Dnmt3b*$^{-/-}$ ES cells transfected with mock, wild-type Dnmt3b or mutant Dnmt3b (S277P and VW-RR). *P* values calculated with Wilcoxon rank-sum test. **d**, Pie chart showing the percentage of transcripts with $\log_2$ fold change (FC) $>1, <-1$ or between -1 and 1. **e**, **f**, Histogram and western blot showing mRNA and protein levels of *Dis3* and *Rrp6* genes in control or Dis3/Rrp6 double knockdown (dKD) in *Dnmt3b*$^{-/-}$ ES cells. β-Actin was used as protein loading control. **g**, Box plots showing the number of total TSSs per gene on RefSeq-annotated TSSs and gene bodies in control or Dis3/Rrp6 dKD *Dnmt3b*$^{-/-}$ ES cells. *P* values calculated with Wilcoxon rank-sum test. **h**, Box plot of the normalized DECAP-seq read counts (RPM) on the intragenic TSSs in the indicated samples. *P* values calculated with Wilcoxon rank-sum test. **i**, Scatter plots of the $\log_2$ RPM values on canonical annotated TSSs ($\pm$100 bp) of the indicated samples. **j**, Venn diagrams of intragenic TSSs with a DECAP-seq signal RPM >6 showing the single-base resolution overlap between the DECAP-seq experiment replicates performed in *Dnmt3b*$^{-/-}$ ES cells. *P* values calculated with Hypergeometric Distribution test. **k**, Pie charts of the DECAP-seq reads distribution on TSSs RPM >6 in control (left) and Dis3/Rrp6 KD (right) *Dnmt3b*$^{-/-}$ ES cells. In green are shown the novel TSSs that overlap with RefSeq annotated TSSs; in yellow, all the common TSSs distributed on gene bodies; and in pink, the sample-specific TSSs on gene bodies. **l**, Scatter plots of the $\log_2$ RPKM gene values in the indicated samples. **m**, Genomic views of the RNA-seq mapped reads from the indicated samples. **n**, Box plots of the ratio between normalized poly(A)$^+$ RNA-seq read counts (RPKM) for the second and the first exon, the third and the first exon, the average of the intermediates (from the fourth to the penultimate exons) and the first exon, and the last and the first exon in wild-type (rep #2) and *Dnmt3b*$^{-/-}$ (rep #2 and clone B77) ES cells. *P* values calculated with Wilcoxon rank-sum test. **o**, Pie-chart showing the percentage of transcripts with an intermediate to first exon ratio (in *Dnmt3b*$^{-/-}$ rep #2 and clone B77 poly(A)$^+$ RNA-seq) versus an intermediate to first exon ratio (in wild-type rep #2 poly(A)$^+$ RNA-seq) $\log_2$ fold change $>1, <-1$ or between -1 and 1. **p**, Box plots showing the number of total TSSs per gene on RefSeq-annotated TSSs and gene bodies identified by DECAP-seq in the indicated RNA compartments. *P* values calculated with Wilcoxon rank-sum test. **q**, Scatter plots of the $\log_2$ RPM values on canonical annotated TSSs ($\pm$100 bp) in the indicated RNA compartments. **r**, Venn diagram of the common intragenic TSSs (defined as having RPM >6 in both *Dnmt3b*$^{-/-}$ and wild-type ES cells) in the indicated RNA compartments. **s**, Box plot of the normalized DECAP-seq read counts (RPM) on the common intragenic TSSs (RPM >6) in the indicated RNA compartments.

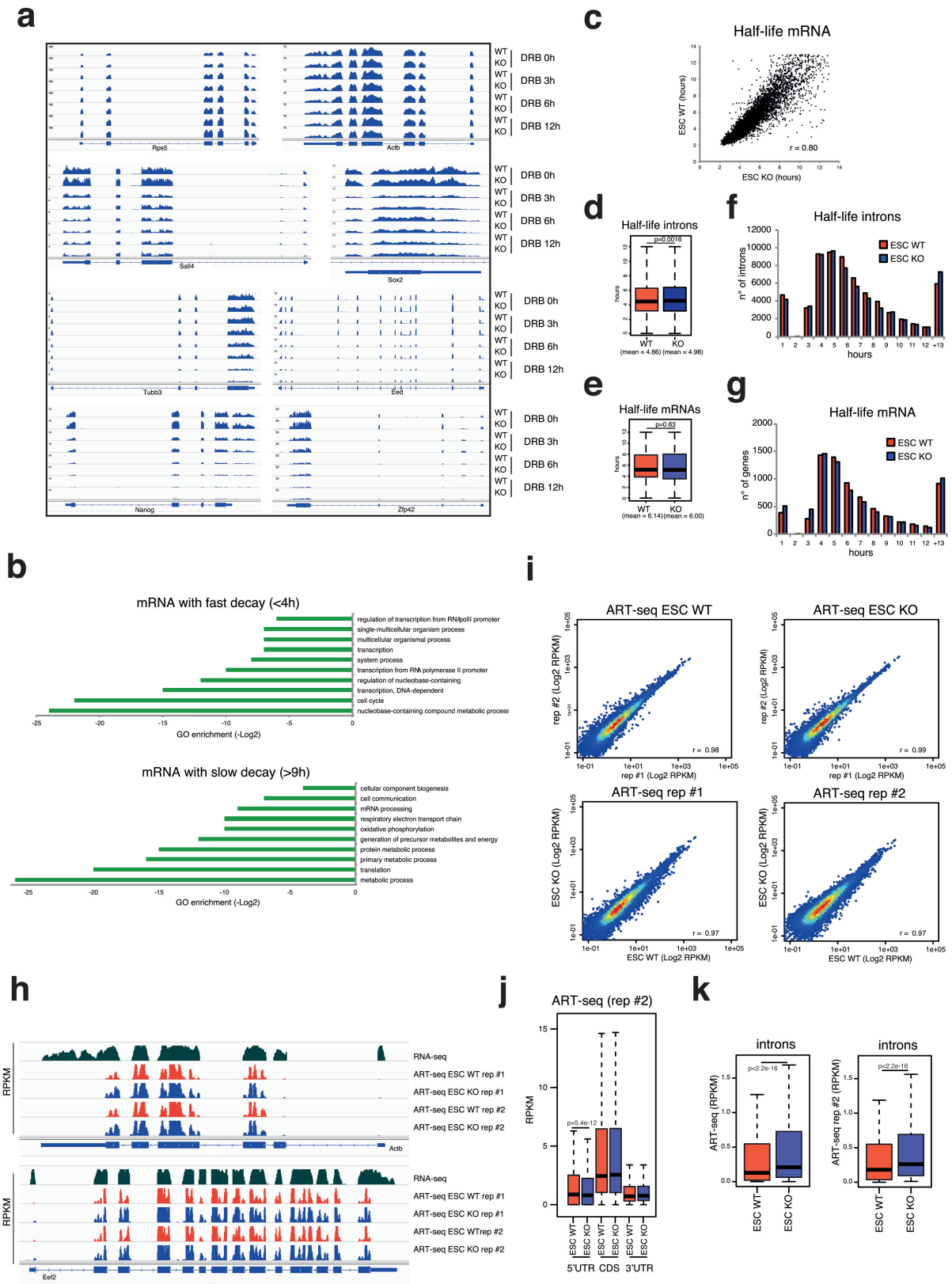

Extended Data Figure 11 | See next page for caption.

Extended Data Figure 11 | Loss of Dnmt3b generates partial intragenic starting RNAs that are as stable as canonical mRNAs. a, Genomic views of the RNA-seq mapped reads from the indicated samples. Genes with slow, medium and fast decay are shown. **b**, Gene Ontology (GO) analysis of the subsets of the mRNAs with fast decay (half-life lower than four hours) or slow decay (half-life higher than nine hours) in wild-type ES cells. The analysis revealed that fast-decay mRNAs are mainly involved in cell cycle and transcription biological processes, while slow-decay mRNAs are related to metabolism and translation. This result is in agreement with that previously observed in mouse ES cells[54,55], supporting the bona fide nature of the experiment. **c**, Scatter plot of mRNA half-life (in hours) in wild-type and *Dnmt3b*$^{-/-}$ ES cells. **d**, **e**, Box plots of intron half-life (in hours) in wild-type and *Dnmt3b*$^{-/-}$ ES cells. Intron half-life is estimated by considering only the reads mapped to intronic regions. Intron half-life is generally lower than mRNA half-life, suggesting lower stability of the RNAs containing intronic parts. Intron half-life calculated in *Dnmt3b*$^{-/-}$ ES cells is significantly ($P = 0.0016$) higher than in wild-type ES cells. *P* values calculated with Wilcoxon rank-sum test. **f**, **g**, Frequency distribution of introns and mRNA half-life among all introns in wild-type and *Dnmt3b*$^{-/-}$ ES cells. **h**, Genomic views of the RNA-seq mapped reads from the indicated samples. ART-seq reads derived only from the coding sequences (CDS) of the mRNAs. RNA-seq is shown as reference example. **i**, Scatter plots of the $\log_2$ RPKM gene values in the indicated samples. **j**, Box plot of the normalized ART-seq rep #2 read counts (RPKM) on the indicated RNA regions in wild-type and *Dnmt3b*$^{-/-}$ ES cells. **k**, Box plot of the normalized ART-seq read counts (RPKM, for both the biological replicates) on the introns in wild-type and *Dnmt3b*$^{-/-}$ ES cells. *P* values calculated with Wilcoxon rank-sum test.

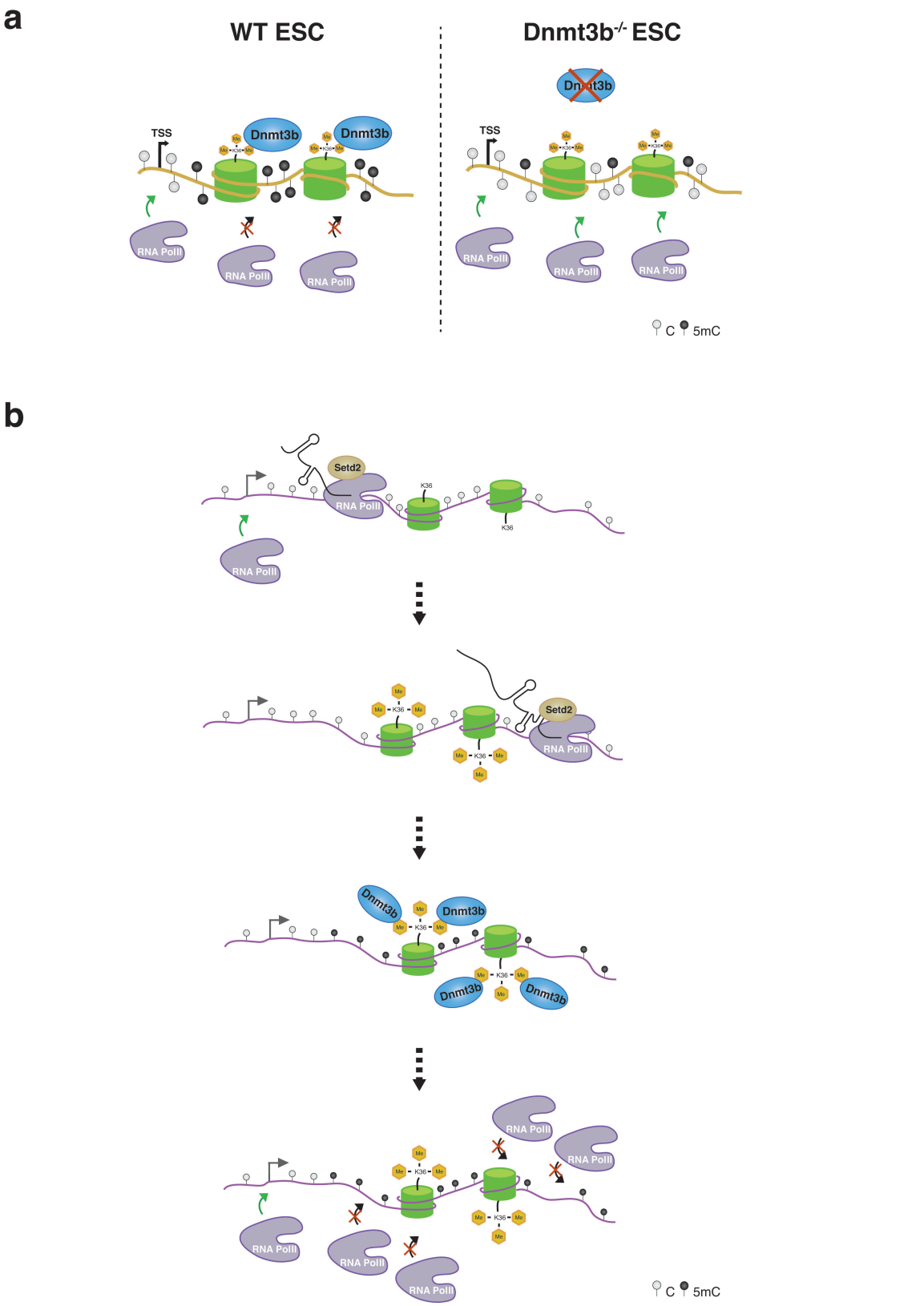

Extended Data Figure 12 | Models from the obtained results. **a**, Scheme of the functional role of the Dnmt3b-dependent intragenic DNA methylation in ES cells. In wild-type cells, Dnmt3b is able to methylate gene bodies to favour a repressive chromatin environment that inhibits spurious entries of Pol II. In the absence of Dnmt3b, gene bodies are hypomethylated, leading to Pol II intragenic entries that generate intragenic transcription initiation. **b**, Epigenetic crosstalk between Pol II, SetD2 and Dnmt3b and relative H3K36me3 and 5mC chromatin modifications unveils how Pol II, through the transcription elongation process, triggers a safety mechanism to ensure its transcription initiation fidelity.